Quarterly Technical Report

Solid State Research

2001:1

Lincoln Laboratory

MASSACHUSETTS INSTITUTE OF TECHNOLOGY

LEXINGTON, MASSACHUSETTS

20010912 101
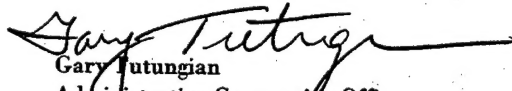
The ESC Public Affairs Office has reviewed this report, and it is releasable to the National Technical Information Service, where it will be available to the general public, including foreign nationals.

This technical report has been reviewed and is approved for publication.

FOR THE COMMANDER

Gary Tutungian
Administrative Contracting Officer
Plans and Programs Directorate
Contracted Support Management

Massachusetts Institute of Technology
Lincoln Laboratory

Solid State Research

Quarterly Technical Report

1 November 2000 — 31 January 2001

Issued 7 September 2001

Lexington   Massachusetts

ABSTRACT

This report covers in detail the research work of the Solid State Division at Lincoln Laboratory for the period 1 November through 31 January 2001. The topics covered are Quantum Electronics, Electro-optical Materials and Devices, Submicrometer Technology, Biosensor and Molecular Technologies, Advanced Imaging Technology, Analog Device Technology, and Advanced Silicon Technology. Funding is provided by several DoD organizations—including the Air Force, Army, BMDO, DARPA, Navy, NSA, and OSD—and also by the DOE, NASA, and NIST.

TABLE OF CONTENTS

LIST OF ILLUSTRATIONS

LIST OF ILLUSTRATIONS (Continued)

LIST OF ILLUSTRATIONS (Continued)

LIST OF TABLES

INTRODUCTION

1. QUANTUM ELECTRONICS

Miniature gain-switched $Ti:Al_2O_3$ lasers, with a cavity length of less than 1 cm, have produced sub-nanosecond pulses with tens of kilowatts peak power, and can be tuned over several tens of nanometers. The combination of performance and size provided by these systems has no precedent in broadly tunable solid state lasers.

2. ELECTRO-OPTICAL MATERIALS AND DEVICES

Mode locking has been demonstrated in an experimental configuration comprising a semiconductor section containing separate gain and modulator regions, and an external section containing a grating mounted in a Littrow configuration. Output pulse widths in the range from 50 to 100 ps and pulse repetition rates between 500 and 780 MHz were obtained.

3. SUBMICROMETER TECHNOLOGY

An experimental dual-detector ion mobility spectrometer (IMS) system has been built to assess the improvements in detection selectivity available when complementary detector channels are used. One channel is based on conventional IMS technology using a β-emitter as an ionization source, while the other channel is based on a novel laser-induced multiphoton ionization technique.

4. BIOSENSOR AND MOLECULAR TECHNOLOGIES

A versatile system for generating B-cell lines has been developed to be used for identification of biological agents. We have produced B cells that express antibodies specific for both viruses and bacteria (foot-and-mouth disease virus and *Francisella tularensis*) and have demonstrated excellent sensitivity, specificity, and reaction time with actual agents.

5. ADVANCED IMAGING TECHNOLOGY

A 512×512-pixel, multiframe charge-coupled device (CCD) imager has been designed and fabricated that collects up to four time-sequential image frames at megahertz rates before having to be read out. Initial measurements on back-illuminated CCDs have demonstrated good isolation between the four captured frames.

6. ANALOG DEVICE TECHNOLOGY

In 100% of chips tested with a critical current density of 10 kA/cm^2, the cross-chip critical current density has been shown to vary by <1%. This level of cross-chip uniformity in critical current density is

required for any process with which one hopes to generate highly integrated 100-GHz clock speed, Josephson junction based electronics.

7.   ADVANCED SILICON TECHNOLOGY

A merged CCD/silicon-on-insulator–CMOS (SOI-CMOS) technology has been developed that enables the fabrication of monolithic, low-power imaging systems on a chip. An integrated image sensor with charge-domain analog-to-digital conversion and on-chip clocking is demonstrated for the first time.

REPORTS ON SOLID STATE RESEARCH

1 NOVEMBER 2000 THROUGH 31 JANUARY 2001

PUBLICATIONS

A New CCD Designed for Curvature Wavefront Sensing	J. W. Beletic* R. J. Dorn* T. Craven-Bartle* B. E. Burke	In *Optical Detectors for Astronomy II,* P. Amico and J. Beletic, eds. (Kluwer, Norwell, Mass., 2000), pp. 283-309
CCD Imager Technology Development at Lincoln Laboratory	B. E. Burke J. A. Gregory A. H. Loomis C. C. Cook D. J. Young M. J. Cooper T. A. Lind G. A. Luppino* J. L. Tonry*	In *Optical Detectors for Astronomy II,* P. Amico and J. Beletic, eds. (Kluwer, Norwell, Mass., 2000), pp. 187-199
Resonant-Tunneling-Diode Relaxation Oscillator	C-L. Chen R. H. Mathews L. J. Mahoney S. D. Calawa J. P. Sage K. M. Molvar C. D. Parker P. A. Maki T. C. L. G. Sollner	*Solid-State Electron.* **44**, 1853 (2000)

*Author not at Lincoln Laboratory.

Evolution of Deep Centers in GaN Grown by Hydride Vapor Phase Epitaxy	Z-Q. Fang* D. C. Look* J. Jasinski* M. Benamara* Z. Lilienthal-Weber* R. J. Molnar	*Appl. Phys. Lett.* **78**, 332 (2001)
Polymer Photochemistry at Advanced Optical Wavelengths	T. H. Fedynyshyn R. R. Kunz R. F. Sinta R. B. Goodman S. P. Doran	*J. Vac. Sci. Technol. B* **18**, 3332 (2000)
Sub-100 nm Silicon on Insulator Complementary Metal-Oxide Semiconducuctor Transistors by Deep Ultraviolet Optical Lithography	M. Fritze J. A. Burns P. W. Wyatt C. K. Chen P. M. Gouker C-L. Chen C. L. Keast D. K. Astolfi D-R. W. Yost D. M. Preble A. V. Curtis P. V. Davis S. G. Cann S. J. Denault H. Y. Liu	*J. Vac. Sci. Technol. B* **18**, 2886 (2000)
Spectroscopy of Competing Mechanisms Generating Stimulated Emission in Gallium Nitride	W. D. Herzog* G. E. Bunea* M. S. Ünlü* B. B. Goldberg* R. J. Molnar	*Appl. Phys. Lett.* **77**, 4145 (2000)
Room-Temperature Testing for High Critical-Current-Density Josephson Junctions	M. J. O'Hara K. K. Berggren	*IEEE Trans. Appl. Supercond.* **10**, 1669 (2000)

*Author not at Lincoln Laboratory.

Solid-Source Molecular-Beam Epitaxy for Monolithic Integration of Laser Emitters and Photodetectors on GaAs Chips	P. A. Postigo* C. G. Fonstad* S. S. Choi W. D. Goodhue	*Appl. Phys. Lett.* **77**, 3842 (2000)
Low Frequency Noise in *n*-GaN with High Electron Mobility	S. L. Rumyantsev* D. C. Look* M. E. Levinshtein* M. A. Khan* G. Simin* V. Adivarahan* R. J. Molnar M. S. Shur*	*Mater. Sci. Forum* **338-342**, 1603 (2000)
Patterning of Sub-50-nm Dense Features with Space-Invariant 157-nm Interference Lithography	M. Switkes M. Rothschild T. M. Bloomstein	*Appl. Phys. Lett.* **77**, 3149 (2000)
60-Gb/s Optically Time-Division Multiplexed Link with All-Optical Demultiplexing	T. G. Ulmer M. C. Gross* K. M. Patel* J. T. Simmons* P. W. Juodawlkis B. R. Washburn* W. S. Astar* A. J. SpringThorpe* R. P. Kenan* C. M. Verber* S. E. Ralph*	*J. Lightwave Technol.* **18**, 1964 (2000)
Dislocation Density in GaN Determined by Photoelectrochemical and Hot-Wet Etching	P. Visconti* K. M. Jones* M. A. Reschikov* R. Cingolani* H. Morkoç* R. J. Molnar	*Appl. Phys. Lett.* **77**, 3532 (2000)

---

*Author not at Lincoln Laboratory.

ACCEPTED FOR PUBLICATION

Temperature Dependence of the Breakdown Voltage for Reverse-Biased GaN p-n-n$^+$ Diodes	R. L. Aggarwal I. Melngailis S. Verghese R. J. Molnar M. W. Geis L. J. Mahoney	*Solid State Commun.*
Gallium Nitride Avalanche Photodiodes Achieve UV Photon Counting	K. A. McIntosh J. Mahoney K. M. Molvar K. Connors R. J. Molnar	*III-V's Review* (Elsevier, Oxford)
Impurity Band in the Interfacial Region of GaN Films Grown by Hydride Vapor Phase Epitaxy	R. J. Molnar J. W. P. Hsu* D. V. Lang* R. N. Kleiman* M. Sergent* D. C. Look*	*J. Electron. Mater.*
Surface Morphology and Electronic Properties of Dislocations in AlGaN/GaN Heterostructures	R. J. Molnar J. W. P. Hsu* M. J. Manfra* D. V. Lang* W. Baldwin* L. N. Pfeiffer*	*J. Electron. Mater.*

PRESENTATIONS[†]

Controlled Contamination and Cleaning of Optical Elements in 157-nm Lithography	V. Liberman T. M. Bloomstein M. Rothschild	Lambda Physik 157-nm Symposium, Fort Lauderdale, Florida, 2 November 2000

---

*Author not at Lincoln Laboratory.

[†] Titles of presentations are listed for information only. No copies are available for distribution.

Plasma-Induced Effects on the Thermal Conductivity of Hydride Vapor Phase Epitaxy Grown N-GaN/Sapphire (0001)	D. I. Florescu* F. H. Pollak* W. B. Lanford* I. Adesida* R. J. Molnar	2000 Fall Meeting of the Materials Research Society, Boston, Massachusetts, 27 November–1 December 2000
Infrared Absorption and Confocal Raman Studies of N-Type GaN Films	J. W. P. Hsu* C. Gmachi* M. J. Matthews* H. M. Ng* A. Y. Cho* R. J. Molnar	2000 Fall Meeting of the Materials Research Society, Boston, Massachusetts, 27 November–1 December 2000
Nature of Highly Conducting Interfacial Layer in HVPE Grown GaN Films	J. W. P. Hsu* D. V. Lang* S. Richter* R. N. Kleiman* A. M. Sergent* R. J. Molnar	2000 Fall Meeting of the Materials Research Society, Boston, Massachusetts, 27 November–1 December 2000
Dislocation Electrical Activity in AlGaN/GaN Heterostructures	D. V. Lang* M. Manfra J. W. P. Hsu* S. Richter* A. M. Sergent* R. N. Kleiman* L. N. Pfeiffer* R. J. Molnar	2000 Fall Meeting of the Materials Research Society, Boston, Massachusetts, 27 November–1 December 2000
Observation of the Quantum Hall Effect in High Mobility AlGaN/ GaN Heterostructures Grown by Molecular Beam Epitaxy	M. J. Manfra L. Pfeiffer* K. Baldwin* D. Lang* J. Hsu* K. West* R. J. Molnar	2000 Fall Meeting of the Materials Research Society, Boston, Massachusetts, 27 November–1 December 2000

*Author not at Lincoln Laboratory.

Growth of High Mobility AlGaN/ GaN Heterojunctions by MBE	M. Manfra* H. Stormer* K. West* K. Baldwin* S. Syed* D. Lang* L. Pfeiffer* J. Hsu* G. Chu* C. Gmachi* R. J. Molnar	2000 Fall Meeting of the Materials Research Society, Boston, Massachusetts, 27 November–1 December 2000
Growth and Investigation of GaN/ AlN Quantum Dots	H. Morkoç* M. A. Reshchikov* J. Cui* M. H. Zhang* F. Yun* M. I. Nathan* P. Visconti* R. J. Molnar	2000 Fall Meeting of the Materials Research Society, Boston, Massachusetts, 27 November–1 December 2000
Magnetically Tunable Superconducting Filters with Ferroelectric Trimming	D. E. Oates A. C. Anderson G. F. Dionne	2000 Fall Meeting of the Materials Research Society, Boston, Massachusetts, 27 November–1 December 2000
Highly Selective Photoenhanced Wet Etching of GaN for Device Fabrication and Defects Investigation	P. Visconti* A. Reshchikov* K. M. Jones* M. H. Zhang* J. Cui* F. Yun* D. F. Wang R. Cingolani* H. Morkoç* C. W. Litton* R. J. Molnar	2000 Fall Meeting of the Materials Research Society, Boston, Massachusetts, 27 November–1 December 2000

*Author not at Lincoln Laboratory.

Observation of Spontaneous Vertical Composition Modulation in Epitaxial GaInAsSb	C. A. Wang C. J. Vineis D. R. Calawa P. M. Nitishin	2000 Fall Meeting of the Materials Research Society, Boston, Massachusetts, 27 November–1 December 2000
Microwave Intermodulation Distortion in YBCO Grain Boundary Junctions	H. Xin D. Oates G. Dresselhaus* M. S. Dresselhaus*	2000 Fall Meeting of the Materials Research Society, Boston, Massachusetts, 27 November–1 December 2000
Electric Force Microscopic Study of Surface Structure and Polarization Effects in GaN Thin Films	F. Yun* K. M. Jones* M. A. Reshchikov* J. Cui* M. H. Zhang* A. Sun* A. Baski* H. Morkoç* P. Visconti* R. J. Molnar	2000 Fall Meeting of the Materials Research Society, Boston, Massachusetts, 27 November–1 December 2000
Monolithic 3.3V CCD/SOI-CMOS Imager Technology	V. Suntharalingam B. E. Burke M. J. Cooper D-R. W. Yost P. M. Gouker M. P. Anthony H. Whittington J. P. Sage J. A. Burns S. Rabe C. Chen J. M. Knecht S. G. Cann P. W. Wyatt C. L. Keast	IEEE International Electron Devices Meeting, San Francisco, California, 10-13 December 2000

*Author not at Lincoln Laboratory.

High Efficiency Optically-Pumped Mid-IR Lasers with Integrated Absorbers	G. W. Turner K. Goyal J. Manfra P. J. Foti H. K. Choi*	Physics of Quantum Electronics Meeting, Air Force Research Laboratory, Snowbird, Utah, 7-11 January 2001
Cryogenic Magnetic Properties of Iron Garnets Diluted with Al-In and Ca-V-In	G. F. Dionne D. E. Oates A. C. Anderson M. Hill* E. Hokanson* D. Cruickshank*	8th Joint Magnetism and Magnetic Materials–Intermag Conference, San Antonio, Texas, 8-11 January 2001
An Integrated Superconductive Device Technology for Qubit Control	K. Berggren E. Macedo T. Weir R. Slattery M. O'Hara D. Nakada T. Orlando*	International Conference on Experimental Implementation of Quantum Computation, Sydney, Australia, 16-19 January 2001
Challenges in Laser Technology for NASA Applications	T. Y. Fan	NASA Earth Science Enterprise Technology Planning Workshop, Arlington, Virginia, 23-24 January 2001
Hydride Vapor Phase Epitaxial Growth of III-V Nitride Devices	R. J. Molnar	IEEE Technical Seminar, MIT Lincoln Laboratory, 25 January 2001; BAE Systems Technical Lectures, Nashua, New Hampshire, 26 January 2001

---

*Author not at Lincoln Laboratory.

ORGANIZATION

SOLID STATE DIVISION

D. C. Shaver, *Head*
R. W. Ralston, *Associate Head*
N. L. DeMeo, Jr., *Assistant*
Z. J. Lemnios, *Senior Staff*

J. W. Caunt, *Assistant Staff*
K. J. Challberg, *Administrative Staff*
J. D. Pendergast, *Administrative Staff*

SUBMICROMETER TECHNOLOGY

M. Rothschild, *Leader*
T. M. Lyszczarz, *Assistant Leader*
T. H. Fedynyshyn, *Senior Staff*
R. R. Kunz, *Senior Staff*

Astolfi, D. K.	Krohn, K. E.
Bloomstein, T. M.	Liberman, V.
Cann, S. G.	Mowers, W. A.
DiNatale, W. F.	Palmacci, S. T.
Doran, S. P.	Sedlacek, J. H. C.
Efremow, N. N., Jr.	Spector, S. J.
Forte, A. R.	Switkes, M.
Geis, M. W.	Sworin, M.
Goodman, R. B.	Uttaro, R. S.

QUANTUM ELECTRONICS

A. Sanchez-Rubio, *Leader*
T. Y. Fan, *Assistant Leader*
T. H. Jeys, *Senior Staff*
J. J. Zayhowski, *Senior Staff*

Aggarwal, R. L.	Herzog, W. D.
Daneu, J. L.	Lynch, E. J.
Daneu, V.	O'Brien, P. W.
DiCecca, S.	Ochoa, J. R.
Goyal, A. K.	

ELECTRO-OPTICAL MATERIALS AND DEVICES

J. C. Twichell, *Leader*
G. W. Turner, *Assistant Leader*
D. L. Spears, *Senior Staff*
R. C. Williamson, *Senior Staff*

Betts, G. E.	Huang, R. K.	Mull, D. E.
Calawa, D. R.	Juodawlkis, P. W.	Napoleone, A.
Calawa, S. D.	LaForge, B. E.	Nitishin, P. M.
Connors, M. K.	Liau, Z. L.	Oakley, D. C.
Donnelly, J. P.	Mahoney, L. J.	O'Donnell, F. J.
Goodhue, W. D.	Manfra, M. J.	Plant, J. J.
Hargreaves, J. J.	McIntosh, K. A.	Taylor, P. J.
Harman, T. C.	Missaggia, L. J.	Wang, C. A.
Harris, C. T.	Molnar, R. J.	Younger, R. D.

1. QUANTUM ELECTRONICS

1.1 MINIATURE GAIN-SWITCHED Ti:Al$_2$O$_3$ LASERS

Passively Q-switched microchip lasers are attractive sources for a wide variety of applications. They are small, simple, robust, and low cost, and produce short pulses with high peak power and excellent pulse stability [1]–[4]. The most efficient passively Q-switched devices operate on the 1.064-μm Nd:YAG gain line; frequency diversity is often achieved though harmonic [1]–[5] and parametric conversion [6]–[8]. Harmonic conversion has proven to be very efficient and robust, even for lasers pumped with low-power (~1-W) diode lasers. Parametric conversion requires higher-power lasers, usually pumped with diode-laser arrays, and tends to be less efficient and less robust. Miniature gain-switched lasers, pumped by passively Q-switched microchip lasers, offer an alternative to parametric conversion. They can have much lower thresholds than parametric devices and offer the possibility of extremely compact and robust tunable systems.

This report discusses gain-switched Ti:Al$_2$O$_3$ lasers pumped by the second harmonic of a 1.064-μm passively Q-switched microchip laser. Although Ti:Al$_2$O$_3$ has previously been used in gain-switched lasers, the short laser cavities discussed here, pumped with the short pulses provided by passively Q-switched microchip lasers, lead to much shorter gain-switched output pulses than previously demonstrated. The combination of performance and size provided by these systems has no precedent in broadly tunable solid state lasers.

The shortest pulse that can be obtained from a gain-switched laser is [9]

$$t_{\mathrm{w}} = \frac{8.1 t_{\mathrm{rt}}}{\ln(G_{\mathrm{rt}})} \tag{1.1}$$

where t_{w} is the full width at half-maximum of the output pulse, t_{rt} is the round-trip time of light within the laser cavity, and G_{rt} is the small-signal round-trip gain of the cavity at the time the pulse forms. This minimum pulse width is obtained when the inversion density within the laser cavity at the time the pulse forms is about 3 times above threshold [9]. If the goal is to have a single output pulse extract the maximum amount of energy from each of the pump pulses, this inversion must typically build up in a period that is between 3 and 10 times the output pulse width. Longer pump pulses will lead to multiple output pulses; lower inversion densities will result in inefficient gain extraction.

In terms of material parameters,

$$t_{\mathrm{w}} = \frac{8.1 n}{c n_{\mathrm{i}} \sigma_{\mathrm{eff}}} \frac{l_{\mathrm{opt}}}{n l_{\mathrm{g}}} \tag{1.2}$$

1

where n is the refractive index of the gain medium, c is the speed of light in vacuum, n_i is the inversion density averaged over the volume of the oscillating mode in the gain media, σ_{eff} is the effective gain cross section of an inverted ion, l_{opt} is the optical length of the cavity, and l_g is the length of the gain medium. The first of the two factors on the right-hand side of Equation (1.2) reflects properties intrinsic to the gain media; the second depends on the cavity and reduces to unity with a monolithic design.

The maximum energy that can be extracted in an output pulse is

$$E_p = \zeta V n_i h \frac{c}{\lambda} \tag{1.3}$$

where ζ is the extraction efficiency of the output pulse, V is the volume of the oscillating mode in the gain medium, h is Planck's constant, and λ is the (free-space) wavelength of oscillation. By longitudinally pumping a short gain-switched laser with the output of a passively Q-switched microchip laser (or one of its harmonics), it is possible to obtain subnanosecond pulses with high efficiency.

Ti:Al$_2$O$_3$ is a nearly ideal gain medium for gain-switched laser oscillation in the near infrared. It has a very large gain coefficient, with a peak value of ~3.5×10^{-19} cm^{-2} at 790 nm, and can support oscillation between ~650 and 1100 nm. Additionally, it has a large absorption coefficient at 532 nm, the second harmonic of the 1.064-μm Nd:YAG laser line, and can be grown with a large concentration of active ions.

The Ti:Al$_2$O$_3$ used in all of the experiments described here has an absorption coefficient of 4.2 cm^{-1} at 532 nm and an active ion concentration of ~6×10^{-19} cm^{-3}. It was cut to a length of 2.6 mm, slightly longer than the $1/e$ absorption length. The pump laser was a 39-μJ, 532-nm, frequency-doubled, high-power microchip laser, with a pulse width of 650 ps and a maximum pulse repetition rate of 3 kHz. The intensity of the pump, for the pump spot sizes used, was well below the saturation fluence of the Ti:Al$_2$O$_3$. Unlike in the Cr^{4+}:YAG experiments described previously [10],[11], the inversion density n_i was determined by the pump intensity.

Experiments were performed with the Ti:Al$_2$O$_3$ gain medium prepared in two different ways. For the first set of experiments, the input face was coated to be highly transmitting at the 532-nm pump wavelength and highly reflecting at 800 nm. The opposite face was antireflection coated at 800 nm and transmitted most of the pump light. Two different laser configurations were demonstrated with the gain medium coated in this way. In the first, the output coupler had a 1-cm radius of curvature and 80% reflectivity at 800 nm. The total length of the laser cavity was 6 mm. The laser was longitudinally pumped with the 39-μJ, 532-nm output of the frequency-doubled microchip laser. The $1/e^2$ radius of the pump spot was 48 μm. The $1/e^2$ mode waist ω_0 for the fundamental transverse mode in the gain-switched laser cavity was 36 μm, located at the input face of the Ti:Al$_2$O$_3$. Since the absorption of the Ti:Al$_2$O$_3$ was not saturated, a smaller pump spot would have resulted in shorter output pulses and more efficient operation. However, the input coating on the Ti:Al$_2$O$_3$ was damaged at a pump intensity only slightly higher than that used. The maximum 800-nm pulse energy that could be extracted from the oscillating mode volume is ~11 μJ. The minimum theoretical pulse width for this cavity operating at 800 nm is 400 ps.

2

This laser produced 600-ps output pulses with 11-μJ pulse energy and 16-kW peak power. The build-up time of the output pulse (the time between the peak of the pump pulse and the peak of the output pulse) was 2.4 ns. The far-field profile of the output indicated that the laser was oscillating in the fundamental transverse mode, and the pulse amplitude was stable to better than $\pm 1\%$. The output spectrum of the laser had a full width at half-maximum of 30 nm, centered near 785 nm.

A second variation of the gain-switched Ti:Al$_2$O$_3$ laser used a 5% output coupler with a 5-cm radius of curvature. The gain medium and the pump were the same as for the device just described. The total cavity length was 4.5 cm. The longer cavity allowed for the insertion of frequency-selective elements. With no intracavity frequency-selective element, the bandwidth of the output was 20 nm, centered at 790 nm. A single-plate quartz birefringent filter, inserted at Brewster's angle, reduced the bandwidth to 0.5 nm and allowed the laser to be tuned from 750 to 815 nm. The tuning range of the laser was limited by the free spectral range of the birefringent filter. The addition of an uncoated, 250-μm-thick glass etalon, inserted normal to the optic axis, reduced the bandwidth to below 0.05 nm, the resolution of the spectrometer used for the measurement. The output energy of the laser, operating at 790 nm, was 12 μJ without the intracavity elements, and was reduced by ~10% with the addition of each intracavity component. The pulse width was 15 ns. The build-up time was 30 ns and the transverse mode was TEM$_{00}$.

In the initial experiments, the coatings used limited the performance of the Ti:Al$_2$O$_3$ laser. The coatings on the Ti:Al$_2$O$_3$ were removed and the Ti:Al$_2$O$_3$ was recoated with high-damage-threshold coatings. In addition, the intracavity-face of the Ti:Al$_2$O$_3$ was coated to be antireflecting at 800 nm and highly reflecting at 532 nm, to allow double-pass absorption of the pump light. Both coatings were sufficiently robust that the 39-μJ pump light could be focused to a spot smaller than the cross section of the oscillating mode of the gain-switched cavities. As a result, in the experiments described below, 85% of the incident pump light was absorbed within the oscillating mode volume.

The first laser tested with the recoated gain medium comprised an output coupler with a 1-cm radius of curvature and a reflectivity of 60%. The total cavity length was 3.5 mm. This laser produced 18-μJ output pulses with a pulse width of 350 ps and peak power of 44 kW. The pulse build-up time was 1.2 ns. The spectral width of the output was 12 nm, centered near 775 nm.

The second laser tested with the recoated gain medium was designed to minimize the cavity length while providing for the insertion of a single-plate quartz birefringent filter (a small piece of the filter used in the earlier experiments). This laser is shown in Figure 1-1. It also used an output coupler with a 1-cm radius of curvature and 60% reflectivity. The total cavity length was 8.5 mm. Operating at a center wavelength of 800 nm, this laser produced 17-μJ pulses with a 600-ps pulse width and 24-kW peak power. The pulse build-up time was 2.7 ns. The birefringent filter allowed the laser to be tuned from 750 to 815 nm, limited by the free spectral range of the filter. The bandwidth, operating at 800 nm, was 1.3 nm. Additional intracavity elements could be used to further reduce the bandwidth, if required by the application.
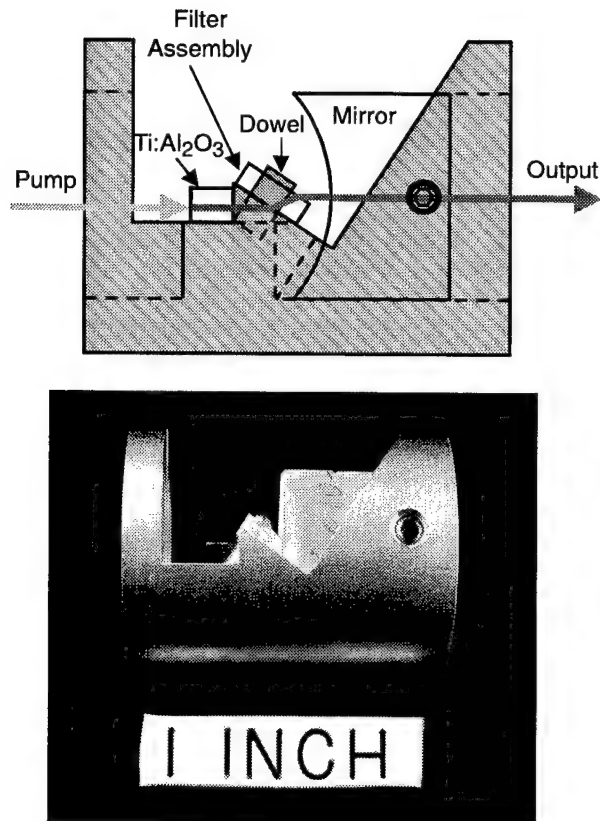
Figure 1-1. Illustration and photograph of miniature gain-switched Ti:Al$_2$O$_3$ laser.

The high peak powers obtained from the miniature gain-switched Ti:Al$_2$O$_3$ lasers will allow efficient harmonic conversion into the visible and ultraviolet. The resulting systems should be extremely robust, as are the harmonically converted passively Q-switched microchip lasers. The wavelength agility of such systems, coupled with their small size, should make them attractive for a wide variety of applications.

The lasers discussed in this report are simple examples of what can be done with this technology. Miniature gain-switched laser systems will continue to be developed to meet the requirements of applications as they emerge.

<div style="text-align:center">

J. J. Zayhowski
A. L. Wilson

</div>

REFERENCES

1. J. J. Zayhowski, *Laser Focus World* **35** (August), 129 (1999).

2. J. J. Zayhowski, *J. Alloys Compounds* **303–304**, 393 (2000).

3. J. J. Zayhowski, *Rev. Laser Eng.* **26**, 841 (1998).

4. J. J. Zayhowski and C. Dill III, *Opt. Lett.* **19**, 1427 (1994).

5. J. J. Zayhowski, *Opt. Lett.* **21**, 588 (1996); erratum, **21**, 1618 (1996).

6. J. J. Zayhowski and A. L. Wilson, *OSA Trends in Optics and Photonics*, Vol. 34, *Advanced Solid State Lasers*, U. Keller, H. Injeyan, and C. Marshall, eds. (Optical Society of America, Washington, D.C., 2000), p. 308.

7. J. J. Zayhowski, *Opt. Lett.* **22**, 169 (1997).

8. J. J. Zayhowski, *IEEE Photon. Technol. Lett.* **9**, 925 (1997).

9. J. J. Zayhowski and P. L. Kelley, *IEEE J. Quantum Electron.* **27**, 2220 (1991); erratum, **29**, 1239 (1993).

10. Solid State Research Report, Lincoln Laboratory, MIT, 2000:3, p. 1.

11. J. J. Zayhowski, S. C. Buchter, and A. L. Wilson, to be published in *OSA Topics in Optics and Photonics, Advanced Solid State Lasers*, C. Marshall and L. R. Marshall, eds. (Optical Society of America, Washington, D.C., 2001).

2. ELECTRO-OPTICAL MATERIALS AND DEVICES

2.1 EXTERNAL CAVITY, ACTIVELY MODE-LOCKED SEMICONDUCTOR LASER OPERATING AT 1.5 μm

Mode-locked lasers, which can produce short optical pulses at high repetition rates, are becoming increasingly important in high-speed systems to transfer and analyze data. Semiconductor mode-locked devices, if they can meet pulse width and pulse jitter requirements, have potential advantages over their solid state or fiber counterparts because of their compactness and high efficiency. Here, we present initial results on an external cavity, actively mode-locked semiconductor laser operating at 1.5 μm.

Three elements are required to achieve active mode locking: optical gain, feedback, and modulation. The external cavity configuration used in these experiments is shown in Figure 2-1. It consists of a semiconductor section, which contains the gain and modulator regions, and an external section, which contains a high-numerical-aperture collimating lens and a grating mounted in a Littrow configuration. The laser cavity and therefore the repetition rate of the laser are determined by the partially reflecting front facet of the semiconductor section and the grating [1].

An expanded view of the semiconductor section is shown in Figure 2-2. A continuous ridge waveguide is used for both the gain and modulator sections. The two sections are electrically isolated using proton bombardment, as discussed below. The waveguide in the gain section is curved to reduce reflection back into the waveguide from the rear facet of the device [2].

351304_2.ai
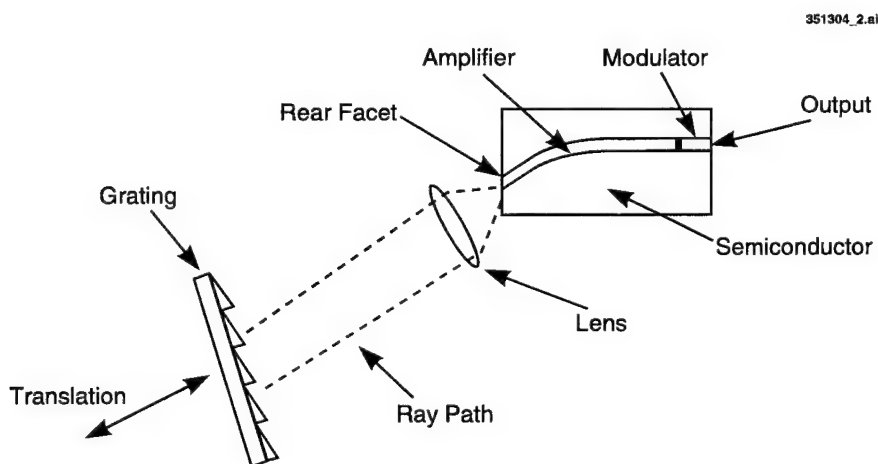
Figure 2-1. External cavity, multiple quantum well semiconductor laser design with Littrow-mounted grating.
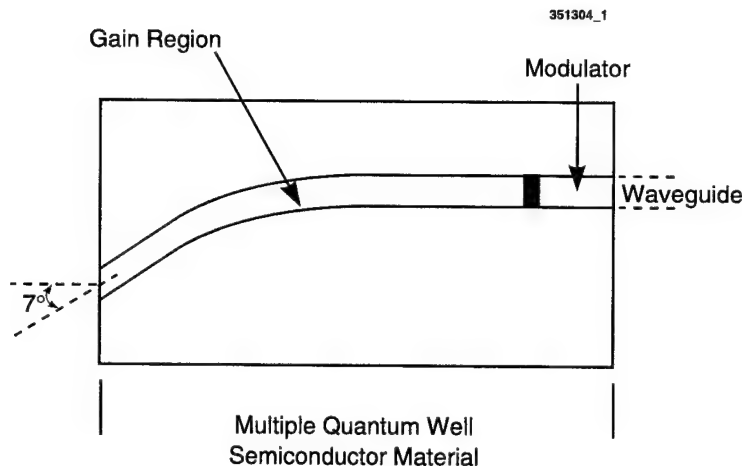
Figure 2-2. Indium phosphide based, multiple quantum well diode with curved ridge waveguide.

The material used to fabricate this device was a stepped graded-index, separate confinement heterostructure with three InGaAsP quantum wells under 1% compressive strain grown by organometallic vapor-phase epitaxy [3]. The p-type InP upper layer contains an etch-stop layer to facilitate the fabrication of the ridge waveguide, used in both the gain section and modulator section. The waveguides are fabricated by etching 10-μm slots on either side of the ridge using a CH_4/H_2 reactive ion etch followed by a short selective wet etch that stops at the etch-stop layer. A thin p^+-InGaAs layer, which is grown atop the p-InP upper cladding to facilitate ohmic contact, is removed everywhere except along the ridge where contact to the gain and modulator sections are to be made. Following top and bottom ohmic contact metallization, the sample is selectively proton bombarded, using photoresist as a bombardment mask, to increase the electrical isolation between the gain and modulator sections and to decrease the parasitic capacitance under the bond pad for the modulator section. Devices nominally 500 μm long with 50-μm-long modulator sections were cleaved out and mounted on Cu heat sinks. The output facet (modulator side) was then coated with a quarter-wave coating, and the rear facet was antireflection coated to further suppress feedback and to increase coupling into the external cavity.

Figure 2-3 is a photograph of the complete laser system. The aluminum plate in the center of the system houses the semiconductor device. The three wires extending from the plate supply the gain bias, modulator drive, and temperature control. The external cavity extends to the left of the photograph, where a lens collects the output from the rear facet and directs it to the grating at the end of the cage assembly, as schematically illustrated in Figure 2-1. To the right of the laser is a coated lensed-fiber pigtail that couples the output from the front facet into an output fiber.

During initial tests of this 1.5-μm laser, we have obtained output pulse widths in the range from 50 to 100 ps and pulse repetition rates between 500 and 780 MHz. The typical average power was 0.25 mW. The

laser repetition rate is easily tuned by changing the length of the external cavity through translation of the grating. The pulse width and power of the laser are highly dependent on the bias conditions. Figure 2-4 is representative of a standard output pulse train as observed using a 45-GHz New Focus photodetector. Spectral analysis reveals an optical bandwidth of 2–3 nm, which is also bias dependent. If the pulses were transform limited, this optical bandwidth could support <1-ps pulses, suggesting a large amount of chirp is present in the system. Efforts are currently under way to quantify the chirp and compensate it either in the cavity or at the laser output to reduce the laser pulse width.

J. J. Plant   J. P. Donnelly
P. W. Juodawlkis   R. J. Bailey
P. J. Taylor   S. H. Groves

REFERENCES

1. M. S. Demokam, *Mode-Locking in Solid-State and Semiconductor Lasers* (Wiley, Great Britain, 1982).

2. R. Helkey, W. Zou, A. Mar, D. B. Young, and J. Bowers, *IEEE Trans. Electron Devices* **40**, 2107 (1993).

3. J. P. Donnelly, J. N. Walpole, S. H. Groves, R. J. Bailey, L. J. Missaggia, A. Napoleone, R. E. Reeder, and C. C. Cook, *IEEE Photon. Technol. Lett.* **10**, 1377 (1998).
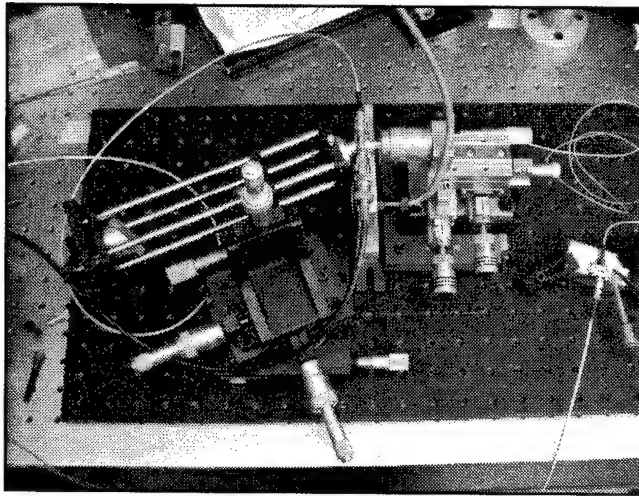
Figure 2-3. Photograph of external cavity, actively mode-locked semiconductor laser.
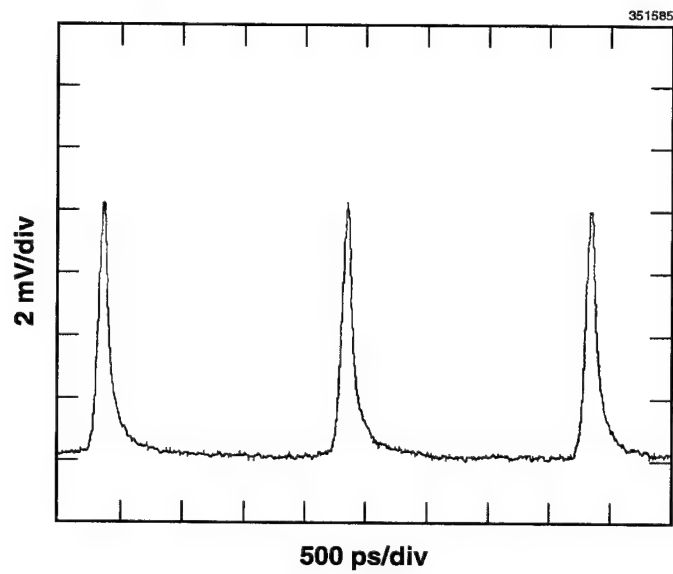
Figure 2-4. Pulse train from semiconductor mode-locked laser observed using 45-GHz New Focus photodetector.

3. SUBMICROMETER TECHNOLOGY

3.1 DUAL-DETECTOR ION MOBILITY SPECTROMETER FOR NARCOTICS DETECTION

Development of an improved means to selectively detect and identify contraband vapors via ion mobility spectroscopy (IMS) has been proposed [1], where the improvements come from using two complementary IMS detector channels in a single instrument package. One detector channel is to be based on the standard IMS technology using a β-emitter as an ionization source and an amine-based dopant gas to induce proton-affinity-based chemical ionization, and the other is to be based on laser-induced multiphoton ionization (MPI) using an aromatic hydrocarbon dopant gas to induce selective chemical ionization based on electron transfer. The two are complementary, as illustrated in Figure 3-1. When the incoming data streams from the two detector channels are fused and processed using a single discrimination algorithm, an increase in the ability to identify particular chemical compounds should be realized. This approach is made both portable and cost effective by the development of Lincoln Laboratory's patented microchip ultraviolet (266 nm) laser, which can deliver peak power densities in excess of 10 MW/cm^2 from a small, portable package.

Previously [1], we had tested aniline as a dopant compound for laser-based chemical ionization. We have also tested xylene, naphthalene, and azulene. Table 3-1 summarizes the key properties of the dopants considered. For the majority of the results shown later in this report, we used naphthalene (chemical formula $C_{10}H_8$), owing to its high resonant one-photon absorbance at 266 nm and its relatively low proton affinity. We felt these characteristics would lead to efficient photoionization and limit the chemical ionization pathways stemming from proton exchange.

Azulene proved to be an interesting compound. It is bright blue in color and absorbs at both the second (532 nm) and fourth (266 nm) harmonic of the principal Nd:YAG wavelength of 1064 nm, adding to the possibility of 2+1 three-photon processes in addition to the standard two-photon process. It yielded the largest dopant peak (~3 V at a concentration of ~1 ppm) but resulted in instrument sensitivity ~10–100 times lower than for naphthalene. This behavior stemmed from its very low ionization potential and the corresponding unfavorable thermodymanics for exchanging charge with compounds whose ionization potentials were higher than its own (azulene's ionization potential is very low at 7.4 eV). This trend suggests that ionization selectivity greater than with naphthalene may be possible without significantly sacrificing sensitivity by substituent-mediated manipulation of the ionization potential of the dopant. Addition of electron-withdrawing substituents such as fluorine tend to increase a compound's ionization potential whereas addition of electron-rich substituents such as alkoxides tend to reduce the ionization potential. By using either naphthalene or azulene as the starting template, dopant gases with ionization potentials and one-photon absorption coefficients custom tailored for electron-mediated charge-exchange ionization should be readily available through the appropriate substituent addition.

11
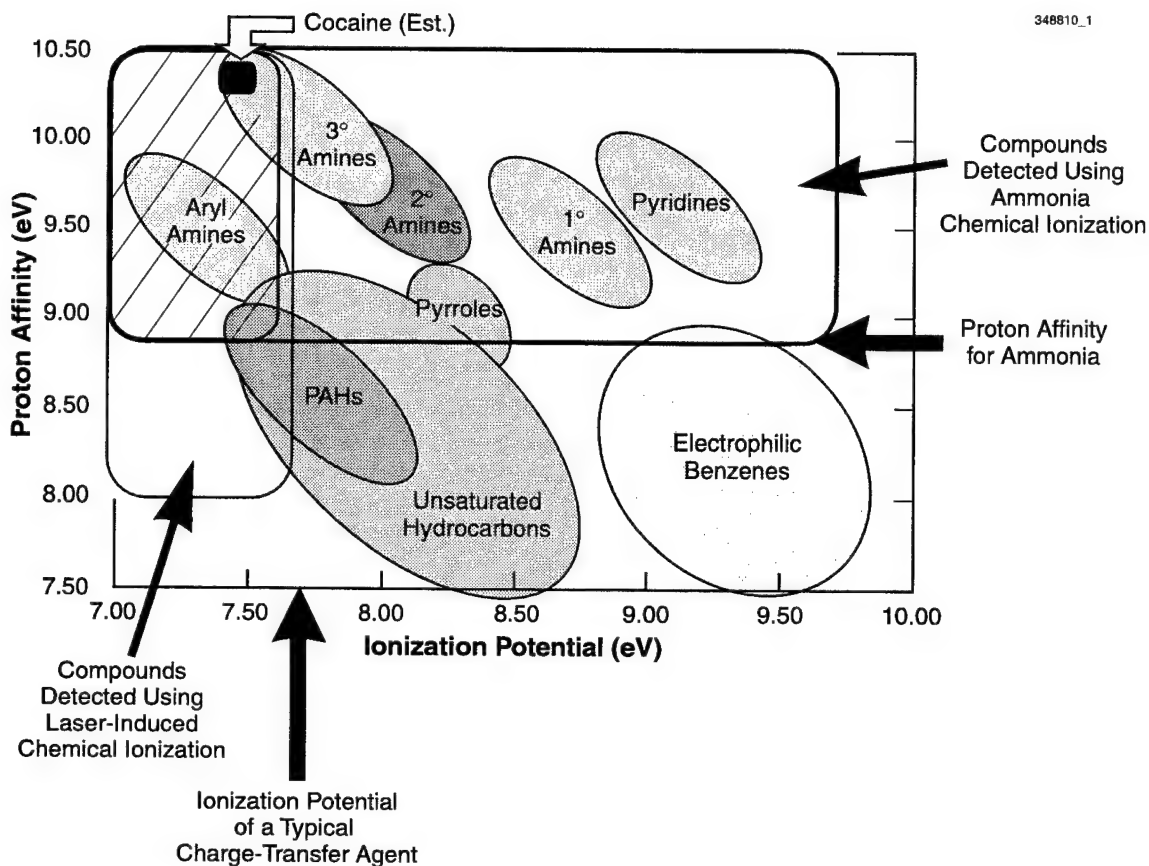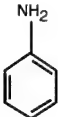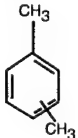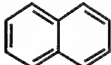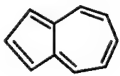
Figure 3-1. Simplified depiction of complementarity of two ion mobility spectrometers based on different ionization principles. In this figure, it is assumed that one detector only detects compounds whose ionization potential is lower than the dopant, whereas the other detector only detects compounds whose proton affinity is higher than that of its dopant gas. The target compounds for detection lie at the intersection of the two detectors' responses.

We have evaluated the characteristics of two separate ion mobility spectrometers operating using different methods of gas-phase ionization. One of the instruments was the Itemizer® provided by Ion Track Instruments (ITI) [2]. Their detector uses a ^{63}Ni β-emitter in combination with an ammonia (NH$_3$) dopant. It is believed that proton attachment is the dominant ionization pathway using this method. The second detector, our home-built system, uses a naphthalene dopant that is selectively ionized via MPI at 266 nm; here it is postulated that electron exchange is the dominant ionization pathway. Since our proposed work will combine these detectors into a single two-channel instrument, we will simply refer to these detection principles as channel 1 and channel 2.

12

TABLE 3-1
Summary of Dopant Chemicals Used for Laser Ionization[a]

Dopant	MW (Da)	Structure	Vapor Pressure[b] (Torr)	Ionization Potential (ev)	Proton Affinity (eV)	OSHA TWA[c] (ppm)
Aniline	93		1	8.05	9.1	2
Xylene	106		8.3	8.57	8.4	100
Naphthalene[d]	128		0.05	8.15	8.47	10
Azulene[e]	128		~0.02	7.4	9.56	None[f]

[a]For the majority of the studies, we used naphthalene for reasons outlined in the text.
[b]At 20°C.
[c]Values here are all comparable to NH_3, which has a time-weighted average (TWA) of 50 ppm.
[d]High absorbance at 266 nm.
[e]High absorbance at both 266 and 532 nm, LD50 (oral), Rat = 4 g/kg.
[f]Although no OSHA TWA levels have been established for azulene, it has been used
as an ingredient in skin creams and the LD50 suggests low toxicity.

The first set of experimental results lists the responses of the two channels to eleven contraband materials as well as to an additional six potential interfering compounds and ten model compounds. These chemicals were introduced into each channel separately and their response functions determined using calibration curves of signal vs mass injected.

Although our original plan was to inject pure vapors of these materials using heated syringes, we could not achieve a satisfactory level of reproducibility for all compounds using this method. As a result, the data shown here were obtained by doing liquid injections from a carrier solvent of either methanol, acetonitrile, or cyclohexane. Typical injection volumes ranged from 0.2 to 5 μL and the analyte quantities ranged from 20 pg to 1 mg, depending on the concentration of the analyte solution. The injector temperatures were between 200 and 220°C for each instrument. The 27 compounds tested are shown in Table 3-2. All chemicals were measured using several injection sizes, and calibration curves of signal vs injection size were assembled for each compound. Table 3-3 lists our findings for the two detectors, whereas Figure 3-2 plots the response of the two detectors against one another as a simple means to determine if they responded in a similar way to each of the tested compounds. From Figure 3-2, it is clear that the detectors responded differently to a wide range of chemicals; in some cases one detector responded with a sensitivity orders of magnitude higher than the other.

Given that the detectors clearly are responding differently we now revisit the proton affinity vs ionization potential chart from Figure 3-1 to determine if the measured sensitivities track with either the compound's proton affinity or ionization potential, as postulated in our original proposal. Figure 3-3 shows the response results for MIT's MPI-$C_{10}H_8$ ionization, and Figure 3-4 shows the results for ITI's ^{63}Ni-NH_3 ionization. Finally, Figure 3-5 shows contours for the ratios in the two detectors' responses as tabulated from the data in Tables 3-2 and 3-3. From these data it is not only apparent that several ionization pathways are competing in each detector, but more important, we can now conclude that we are able to control the dominant ionization pathways in an IMS detector, thereby imparting a unique response signature. Data fusion modeling (not shown) indicates that the detectors' complementarity is sufficient to allow for improved discrimination. The next step of the program is to build a single instrument housing each of the complementary detectors.

R. R. Kunz
W. F. DiNatale

REFERENCES

1. R. R. Kunz, J. J. Zayhowski, P. Becotte-Haigh, and W. J. McGann, *Proceedings of the 1999 Office of National Drug Control International Technology Symposium* (ONDCP, Washington, D.C., 1999).

2. Ion Track Instruments, Wilmington, Mass.

TABLE 3-2

Chemicals Tested Using Both the Lincoln Laboratory Laser-Ionization-Based IMS and the Ion Track Instruments Itemizer IMS Using ^{63}Ni-NH$_3$ Ionization

Compound	Type	Proton Affinity (eV)	Ionization Potential (eV)
1,4-Diaminobutane	Model compound	10.12	8.8
6-Acetyl morphine	Controlled substance		
Acetyl salicylic acid	Model compound	9.0	9.11
Acridine	Potential interferant	10.08	7.85
Anthracene	Model compound	9.00	7.47
Benzoyl ecgonine	Controlled substance		
Benzoyl ecgonine methyl ester (cocaine)	Controlled substance		
Bibenz(a,h)acridine	Potential interferant	10.4	8.07
Bibenz(a,h)anthracene	Potential interferant	9.2	7.39
Diesel oil	Potential interferant		
Ecgonine methyl ester	Controlled substance		
Heroin	Controlled substance		
Lysergic acid diethylamide	Controlled substance		
Methamphetamine	Controlled substance		
Methylenedioxy methamphetamine	Controlled substance		
Morphine	Controlled substance		
Nicotine	Model compound		
Phencyclidine	Controlled substance		
Phenylpropanolamine	Model compound		
Poly(ethylene glycol)	Potential interferant	9.80	9.2
Pyrazine	Model compound	9.09	9.28
Pyrene	Model compound	8.96	7.45
Pyridine	Model compound	9.60	9.66
Quinoline	Model compound	9.85	8.62
Tetrahydrocannibol	Controlled substance		
Toluene	Model compound	8.25	8.82
Vaseline Intensive Care Lotion	Potential interferant		

TABLE 3-3
Summary of Detector Responses Comparing Chemicals Tested

Compound	MW (Da)	Drift Time (ms)	MIT (mC/mole)	Drift Time (ms)	ITI (mC/mole)	Ratio[a]
Benzene	78	4.35	0.0048		0	N/A
Pyridine	79.1	4.87	0.19	4.10	590	0.00032
Pyrazine	80.1	4.50	0.0046	4.50	1.8	0.0026
1,4-Diaminobutane	88	5.45	37	4.51	3100	0.012
Toluene	91	5.00	0.097	4.60	0.0023	42
Naphthalene	128	5.74	N/A	5.5	0.77	N/A
Quinoline	129.2	5.83	37	4.96	340	0.11
Methamphetamine	149	6.58	110	5.65	180	0.61
Nicotine	162	6.76	430	5.72	210	2.0
Anthracene	178	6.58	430	5.70	36	12
Acridine	179	6.77	890	5.67	960	0.93
Acetyl salicylic acid	180	ND	<0.001	6.08	35	<0.000029
Phenylpropanolamine	188	6.67	270	5.68	170	1.6
Methylenedioxy methamphetamine	193	7.25	120	6.03	2000	0.060
Ecgonine methyl ester	199.3	7.28	650	6.12	660	0.98
Poly(ethylene glycol)	200	7.10	48	7.00	660	0.071
Pyrene	202.3	7.00	220	6.20	29	7.6
Phencyclidine	243.4	8.68	1800	7.20	460	3.9
Bibenz(a,h)anthracene	278	8.74	3200	6.29	670	4.8
Bibenz(a,h)acridine	279	8.57	6900	7.32	4300	1.6
Morphine	285.3	8.95	5400	7.40	1400	3.9
Benzoyl ecgonine	289.3	9.24	4600	7.68	1100	4.2
Tetrahydrocannibol	289.3	10.35	3900	8.60	5400	0.72
Benzoyl ecgonine methyl ester (cocaine)	303.4	9.20	6400	7.78	16 000	0.40
Lysergic acid diethylamide	323.4	9.86	9200	8.28	910	10
6-Acetyl morphine	327	9.57	1200	8.30	2400	0.50
Heroin	369.4	10.32	3100	8.78	3400	0.91
Vaseline Intensive Care Lotion	–	6.20 8.0	0.35 7.1	5.37	24	0.015

[a]Ratio of detector responses for the two detectors where values >1 indicate a greater response was obtained for the MIT MPI-$C_{10}H_8$ detector and values <1 indicate a greater response was obtained for the ITI ^{63}NiNH$_3$ detector.
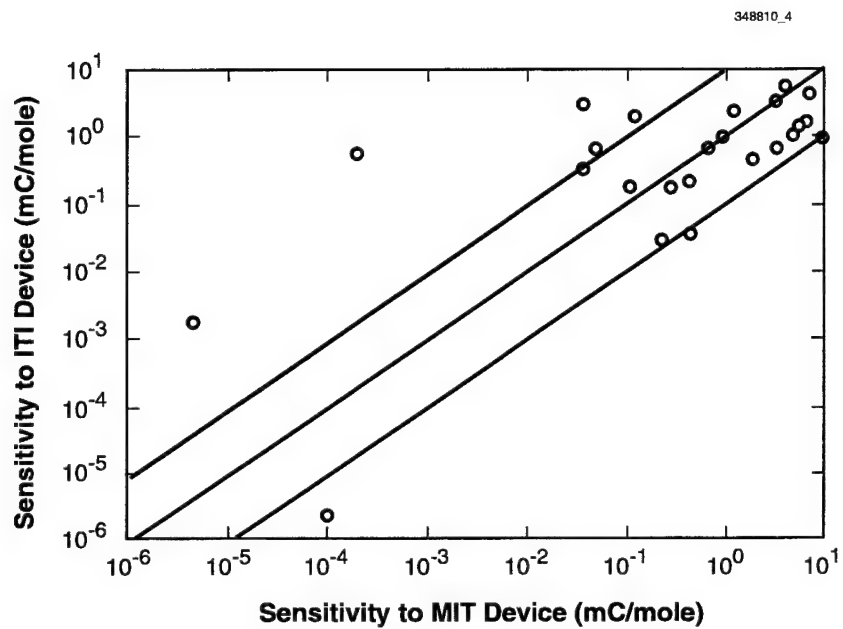
Figure 3-2. ITI's ^{63}Ni-NH$_3$ detector response vs MIT's MPI-C$_{10}$H$_8$ detector response. Data points falling on the center of the three solid lines indicate an identical response in the two detectors. Maximum benefit of the two-channel approach requires the least amount of correlation (i.e., few data points lying on the center line).

17
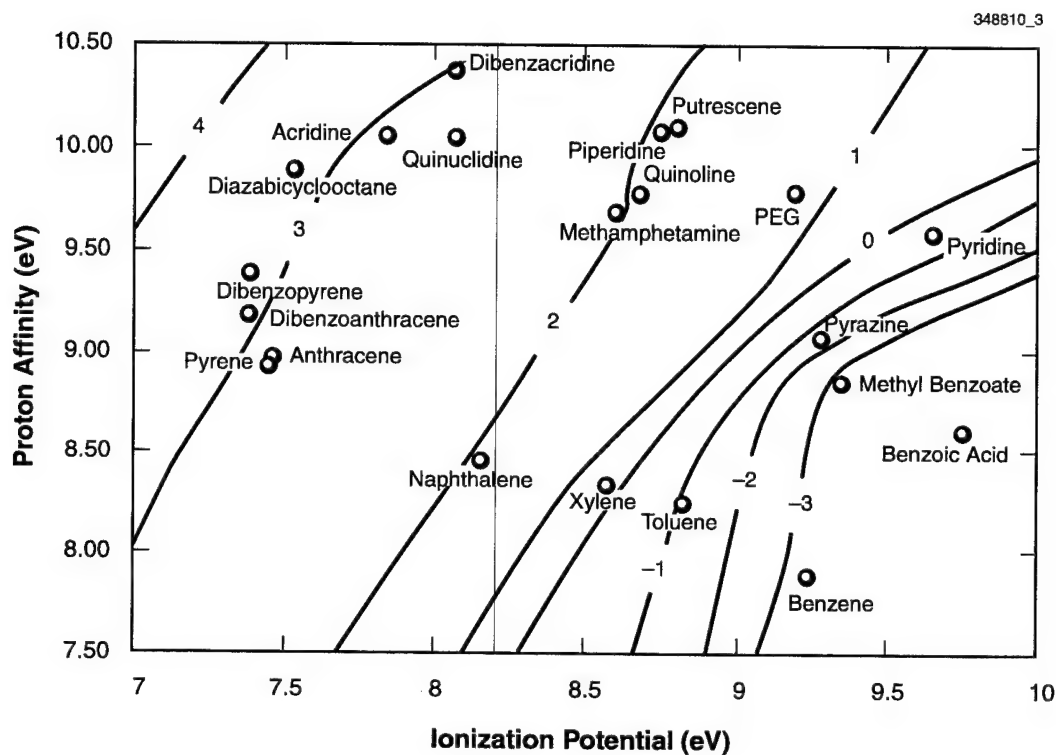
Figure 3-3. Response contours for MIT's MPI-$C_{10}H_8$ laser-ionization detector. The contour lines are in units of log[Response(mC/mole)]. If the signal depended only on the analyte ionization potential, all contour lines would run vertically and the detector response would be near zero at ionization potentials greater than 8.2 eV (thin vertical line). The more horizontal contour lines at ionization potentials >9.5 eV indicate that proton exchange is beginning to dominate in this region, even though absolute sensitivities are low.
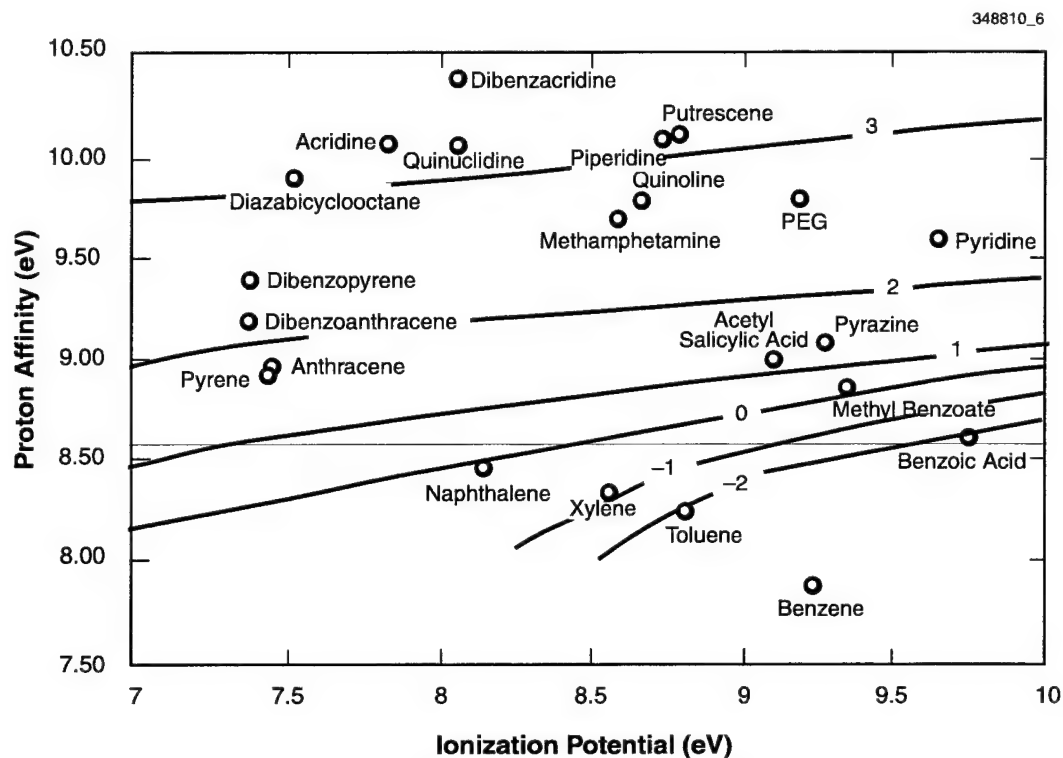
Figure 3-4. Response contours for ITI's ^{63}Ni-NH$_3$ detector. The contour lines are in units of log[Response(mC/ mole)]. If the signal depended only on analyte proton affinity, all contour lines would run horizontally and the detector response would be near zero at proton affinities <8.6 eV (the value for NH$_3$, the thin horizontal line).

19
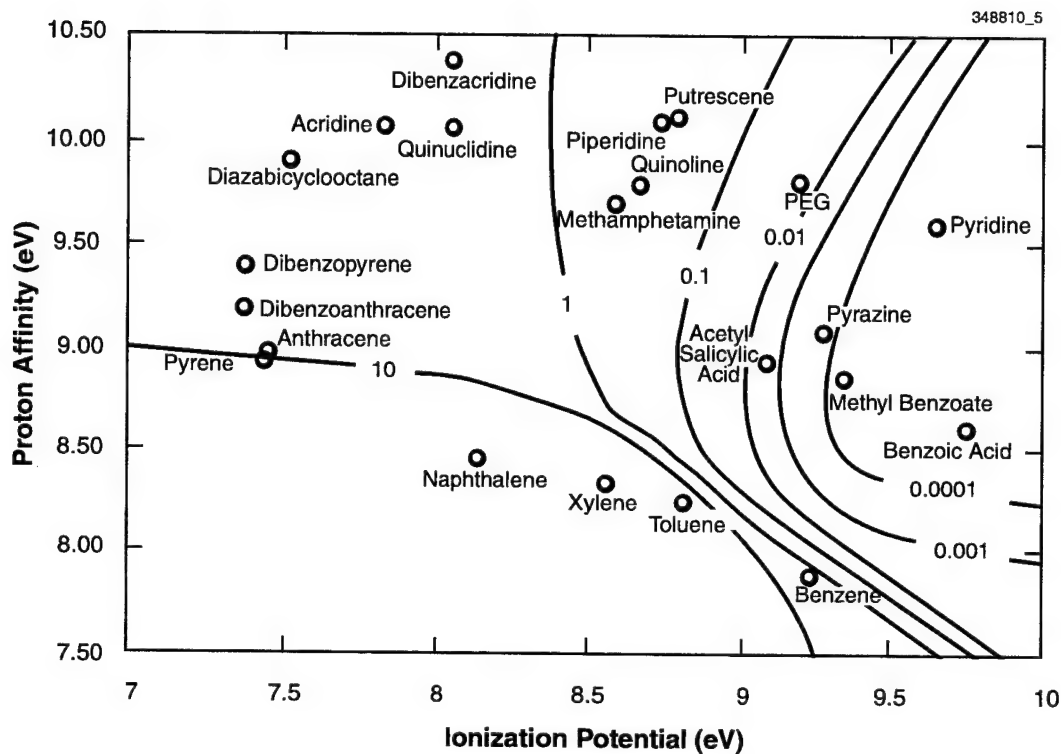
Figure 3-5. Contours showing the ratio in detector responses for MIT's MPI-$C_{10}H_8$ detector and ITI's ^{63}Ni-NH_3 detector. Values greater than one indicate the MIT detector gave a stronger response. For nearly all the contraband materials, the response ratio varied from between 0.1 and 10 (see Figure 3-2).

4. BIOSENSOR AND MOLECULAR TECHNOLOGIES

4.1   DEVELOPMENT OF GENETICALLY ENGINEERED B-CELL LINES THAT RESPOND TO BIOLOGICAL AGENTS

Standard bioagent identification methods include culture techniques, enzyme-linked immunosorbent assay (ELISA), and polymerase chain reaction (PCR). Bacterial culture takes hours to days and a traditional ELISA requires several hours, although recent advances in alternative immunoassays demonstrate equal or better sensitivity in 14 min [1]. Of the three standard methods, PCR is the most rapid at 7 min in a pristine laboratory setting [2]. While these methods are accurate and represent an improvement in rapid detection, there is an increasing demand for techniques that yield faster results without a loss of accuracy [3]. By comparison, B lymphocytes identify foreign substances within seconds. The cross-linking of membrane-bound antibodies by a polyvalent antigen induces a signal transduction cascade, which increases the concentration of cytosolic calcium from internal stores and the environment [4].

In order to develop a pathogen sensor that is specific, sensitive, and faster than current methods, we have harnessed this natural detection and signal amplification system. We have developed an immortal B-cell line that expresses aequorin, a calcium-sensitive bioluminescent protein found in the jellyfish *Aequorea victoria* [5],[6]. Active aequorin consists of the protein, apoaequorin, and its luciferin, coelenterazine, a membrane-permeating luminophore, which can be added to the medium. After binding calcium ions, aequorin undergoes a conformational change causing the oxidation of coelenterazine and the emission of light with a peak wavelength of 469 nm [7],[8]. Aequorin-containing B cells [9] were then engineered to be specific by transfection with expression vectors for recombinant antibodies, and emit light when exposed to the biological agent recognized by the antibody.

Antibodies are protein complexes consisting of two light and two heavy chains, as seen in Figure 4-1. Each chain contains an antigen-binding region (variable region) and an interchangeable constant region. We have developed a recombinant antibody expression vector system in which the DNA encoding the constant regions are permanent components, but the DNA for the variable regions can be exchanged to alter the specificity. The light chain expression vector was constructed by Andrew Bradbury [10] (obtained from Invitrogen), and the heavy chain expression vector was derived from Invitrogen's pDisplay, which was modified to include the heavy chain constant region but exclude the extraneous markers. The antigen-binding variable regions of antibodies are obtained either as DNA sequence from a collaborator, or cloned by reverse transcriptase PCR from the RNA of a hybridoma cell line, and are inserted into the appropriate vector by standard molecular biology techniques.

After aequorin-containing B cells were transfected with recombinant antibody vectors and screened for surface expression of complete antibodies, they were tested for photon emission in the presence of biological agent. B-cell lines with antibodies specific for foot-and-mouth disease virus (FMDV) [11] were

21
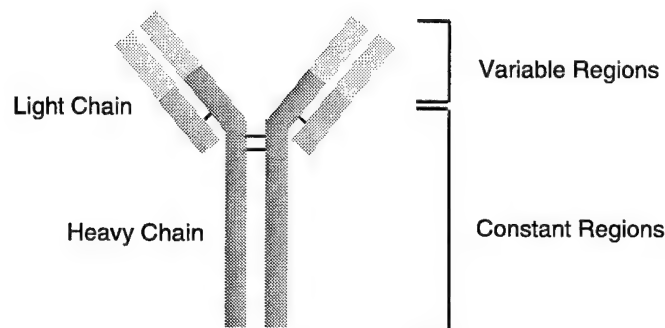
Figure 4-1. Antibody structure.

tested against live FMDV at the USDA BL-3 facility at Plum Island, N.Y., in a commercial luminometer, shown in Figure 4-2. Clones 8, 12, and 31 are different B-cell lines (derived from a single transfected cell) with the same antibody. Similar photon levels are detected from all three B-cell lines in ~40 s, indicating the reproducibility of the system, while there is no signal in the absence of any stimulant (background). Furthermore, there is no luminescence in the presence of a virus with a mutation at a single amino acid (mutant FMDV) that abrogates antibody binding, demonstrating the specificity of the B-cell response. Figure 4-3 illustrates the response of a B-cell line with antibodies specific for *Francisella tularensis* [11], the bacterium that causes tularemia. These experiments were done with inactivated agent, and in a centrifugal format that optimizes B-cell/agent interactions. The agent is centrifuged for 60 s (pre-spin), the B cells added (B-cell loading), and the sample spun for an additional 5 s (spin) to bring the cells into contact with the concentrated agent. The graph shows actual assay time, including sample preparation, and even with these additional steps photon emission is detected in less than 2 min. Specificity is again demonstrated in the absence of any agent (0), and in the presence of another bacterial agent (plague) that is not recognized by the antibody. Finally, the dose response indicates that the sensitivity of the B cells is sufficient to identify approximately 500–5000 bacteria.

In summary, we have developed a versatile system for generating B-cell lines to be used for identification of biological agents. We have produced B cells that express antibodies specific for both viruses and bacteria (FMDV and *Francisella tularensis*) and have demonstrated excellent sensitivity, specificity, and reaction time with actual agents. We are currently expanding our detection capabilities to include pathogens such as *Yersinia pestis* (plague), Venezuelan equine encephalitis virus, cholera, *Brucella spp.*, smallpox virus, and *Bacillus anthracis* (anthrax), and have collaborations with the U.S. Army Medical Research Institute of Infectious Diseases, the Nuclear Medicine Research Council, and the Centers for Disease Control to test the sensor with active agents at BL-3 facilities.

M. S. Petrovick
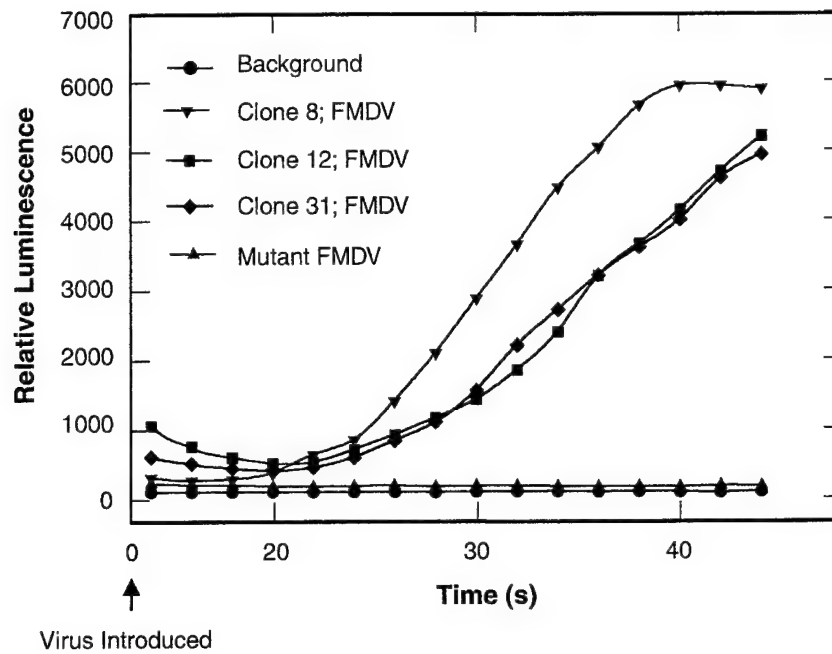
Figure 4-2. B-cell response to foot-and-mouth disease virus.
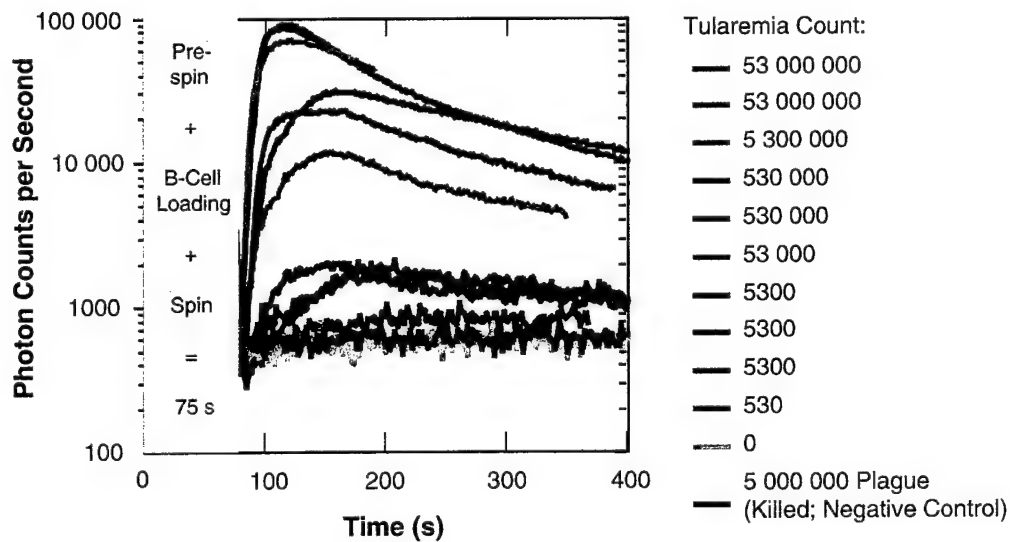
Figure 4-3. Dose response for killed tularemia.

23

REFERENCES

1. C. A. Rowe, S. B. Scruggs, M. J. Feldstein, J. P. Golden, and F. S. Lisler, *Anal. Chem.* **71**, 439 (1999).

2. P. Belgrader, W. Benett, D. Hadley, J. Richards, P. Stratton, R. Mariella, and F. M. Ianovich, *Science* **284**, 449 (1999).

3. D. Ivnitski, I. Abdel-Hamid, P. Atanasov, and E. Wilkins, *Biosensors Bioelectron.* **14**, 599 (1999).

4. H. A. Wilson, D. Greenblatt, M. Poenie, F. D. Finkelman, and R. Y. Tsien, *J. Exp. Med.* **166**, 601 (1987).

5. M. J. Cormier, D. C. Prasher, M. Longiaru, and R. O. McCann, *Photochem. Photobiol.* **49**, 509 (1989).

6. O. Shimomura, B. Musicki, and Y. Kishi, *Biochem. J.* **261**, 913 (1989).

7. F. I. Tsuji, S. Inouye, T. Goto, and Y. Sakaki, *Proc. Natl. Acad. Sci. USA* **83**, 8107 (1986).

8. O. Shimomura and F. H. Johnson, *Proc. Natl. Acad. Sci. USA* **75**, 2611 (1978).

9. D. Button and M. Brownstein, *Cell Calcium* **14**, 663 (1993).

10. L. Persic, M. Righi, A. Roberts, H. R. Hoogenboom, A. Cattaneo, and A. Bradbury, *Gene* **187**, 1 (1997).

11. E. Rieder, A. Berinstein, B. Baxt, A. Kang, and P. W. Mason, *Proc. Natl. Acad. Sci. USA* **93**, 10428 (1996).

5. ADVANCED IMAGING TECHNOLOGY

5.1 BURST-FRAME-RATE CCD IMAGER

A 512 × 512-pixel, multiframe charge-coupled device (CCD) imager has been developed for collecting four sequential image frames at megahertz rates. To operate at fast frame rates with high sensitivity, the imager uses the electronic shutter technology that was developed for back-illuminated CCD imagers [1]. Also required for the megahertz frame rates was metal strapping of the polysilicon gate electrodes in the imaging array. Tested back-illuminated CCD imagers have demonstrated the multiframe capture capability of this detector scheme.

Figure 5-1 is a schematic diagram of the CCD imager device. The imager has a full-frame architecture with the imaging section having 512 × 512 superpixels. Each superpixel is 96 μm square where up to four images can be captured and stored locally in a pixel. As shown in Figure 5-2, the superpixel has 8 (12 × 96 μm) subpixels. A single image frame is captured by two subpixels located 48 μm apart in the superpixel structure. Two subpixels with depletion regions spaced 48 μm apart were needed to limit carrier diffusion in the substrate and collect the photoelectrons in times that were consistent with megahertz frame rates. Figure 5-2 also shows the metal lines located in the pixel that connects to the imaging-array gate electrodes and shutter drain. Typically, the CCD gate electrodes are fabricated using relatively resistive polysilicon lines. For megahertz frame rates, metal strapping of the polysilicon lines was needed to lower the effective RC switching time constant of the imaging-array gate electrodes.
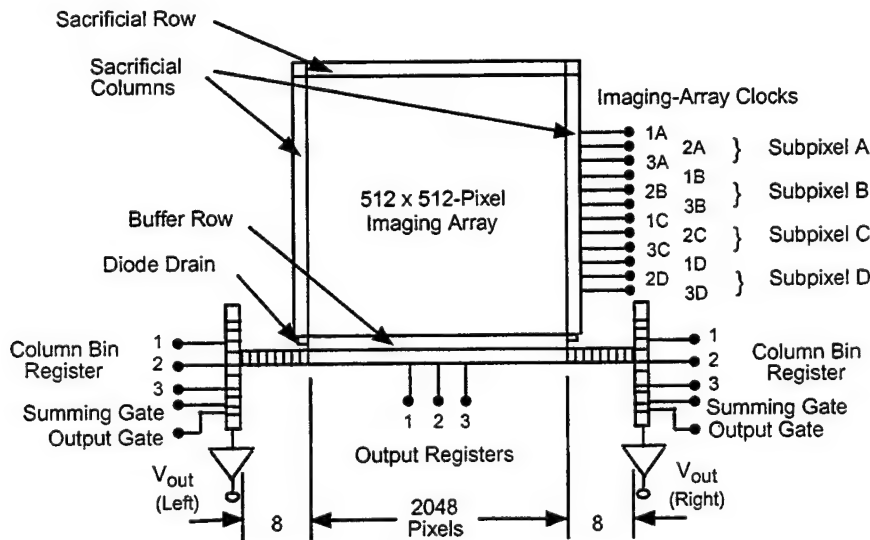
Figure 5-1. Schematic of burst-rate CCD imager.
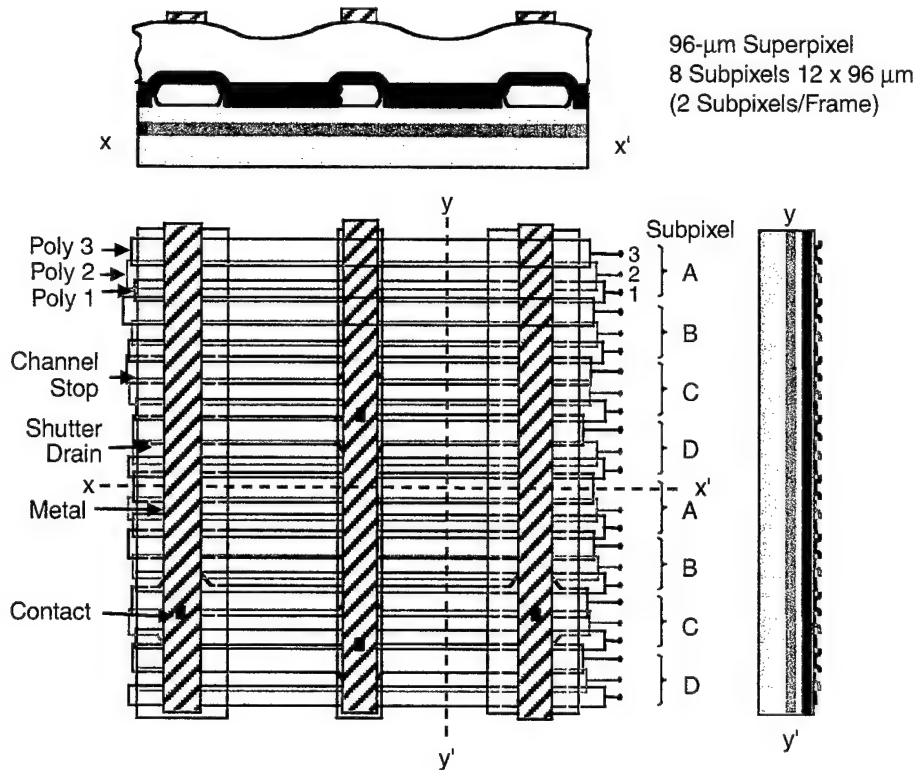
Figure 5-2. Top and cross-sectional views of superpixel showing subpixel locations.

Figure 5-3 shows the shutter operation for capturing four time-sequential image frames. To capture frame 1, phases 1 A and 2 A of two subpixels are taken to a high voltage setting (15–21 V); the other phases 1 B, C, D and 2 B, C, D gate electrodes are set to an intermediate voltage level (6–12 V). Phases 1 A and 2 A collect the photoelectrons created during the first frame time period. The intermediate levels of the other phases 1 B, C, D and phases 2 B, C, D are appropriate for holding the collected signal. Phase 3 is set to a low voltage (–6 to 0 V) to isolate superpixels and subpixels. The second frame is captured by setting phases 1 B and 2 B to the high-voltage level, setting phases 1 A, C, D and phases 2 A, C, D to the middle level, and maintaining a low-voltage setting on phase 3. Phases 1 A and 2 A store the photoelectrons collected during the first frame open period. The remaining frames are captured by continuing this logical sequence. This approach for collecting images at high frame rates is sensitive because of the effective 100% fill factor and back-illuminated quantum efficiency of the CCD imager pixel.

Back-illuminated, burst-rate CCD imagers have been packaged and tested. A focused blue light-emitting diode (LED) light source with a peak response at 460 nm was pulsed on during the first frame shutter open time (frame 1) and turned off for the remaining three frame shutter open times (frames 2, 3,

26
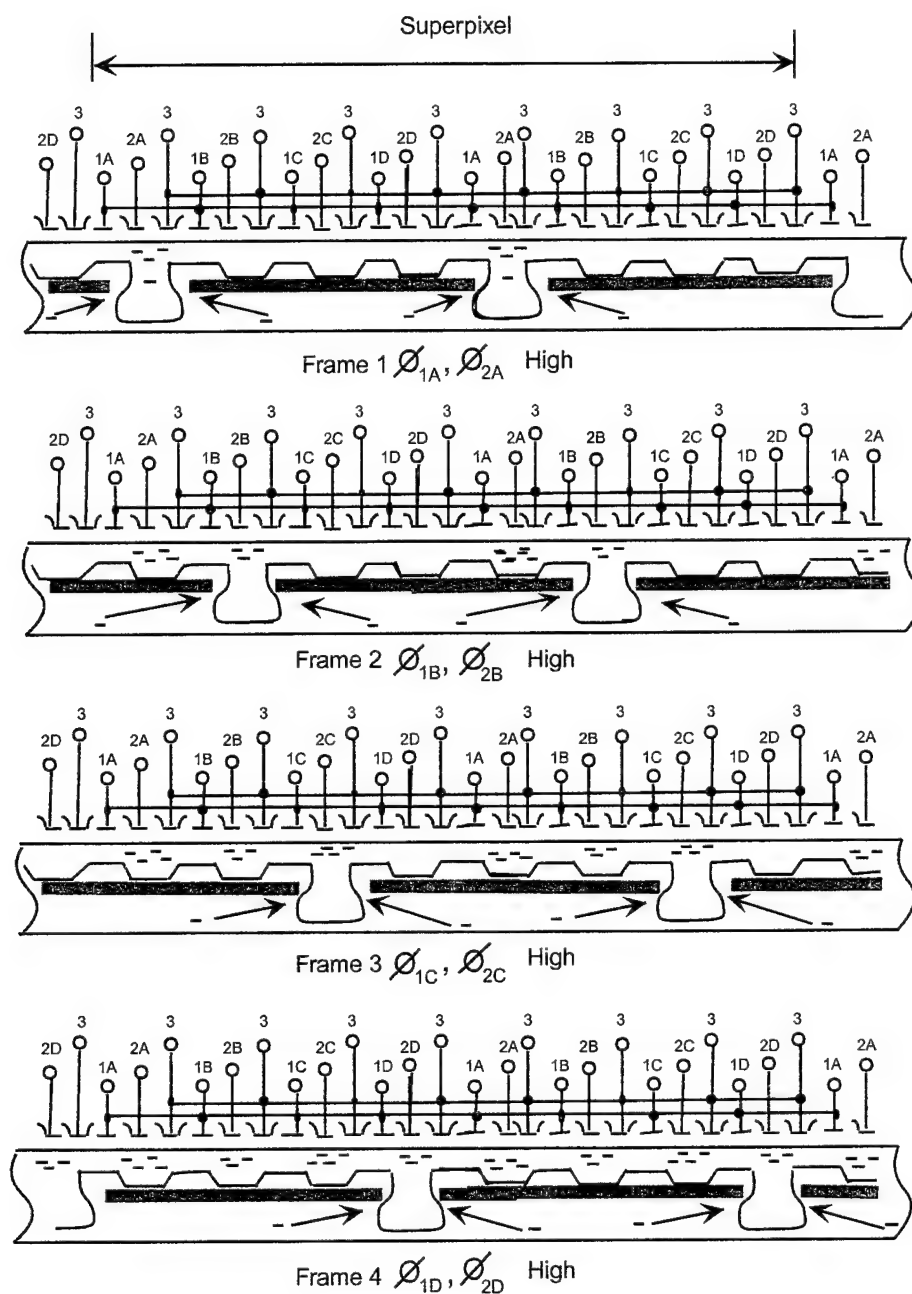
Figure 5-3. Pixel operation for capture of four sequential frames.

27
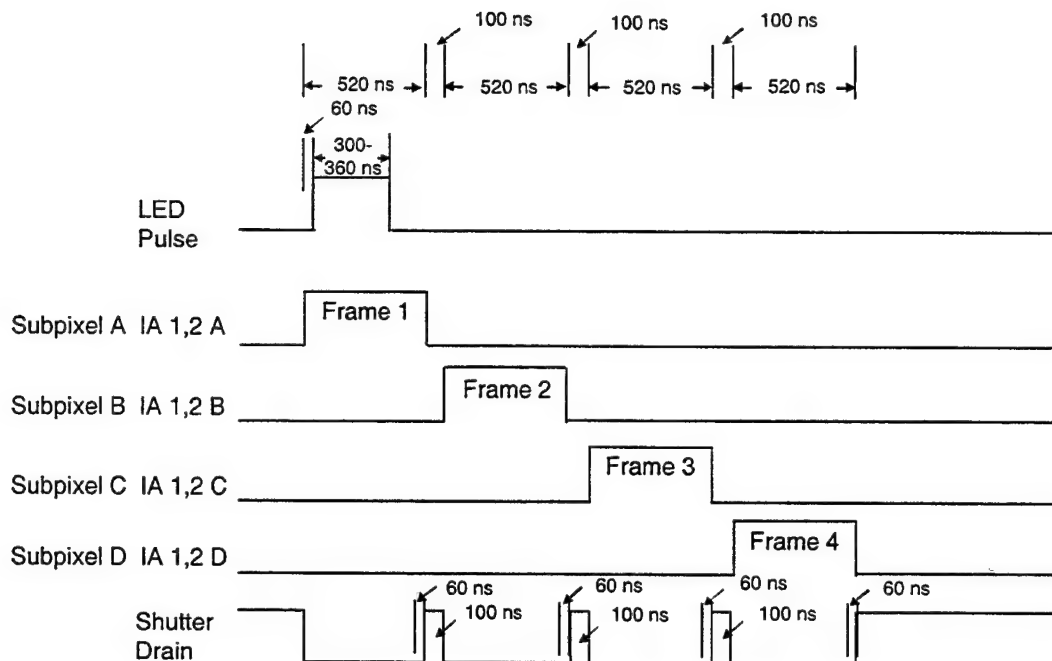
Figure 5-4. Diagram of timing sequence for the light-emitting diode (LED) and the subpixel imaging-array (IA) electrodes.

4). A high-pass filter with a cutoff wavelength of approximately 550 nm was located after the LED to reduce the long-wavelength light signal. Figure 5-4 gives the timing sequence for the LED and the subpixel imaging-array electrodes. Figure 5-5(a) shows areal intensity images of the four frames, and Figure 5-5(b) gives a cross-sectional plot of signal vs row position. The extinction ratio (ratio of photoelectrons measured in subpixel A to photoelectrons measured in subpixel B, C, or D) was greater than 1000 at the highest rate measured of 1.6 MHz.

R. K. Reich   D. M. O'Mara
D. J. Young   A. H. Loomis
D. M. Craig

REFERENCE

1. R. K. Reich, R. W. Mountain, W. H. McGonagle, J. C-M. Huang, J. C. Twichell, B. B. Kosicki, and E. D. Savoye, *IEEE Trans. Electron Devices* **40**, 1221 (1993).

Display Range: 0-20,000 ADU

Subpixel C
Frame 3
Extinction
1157

Subpixel D
Frame 4
Extinction
1659

Subpixel A
Frame 1

Subpixel B
Frame 2
Extinction
2148

(a)

(b)
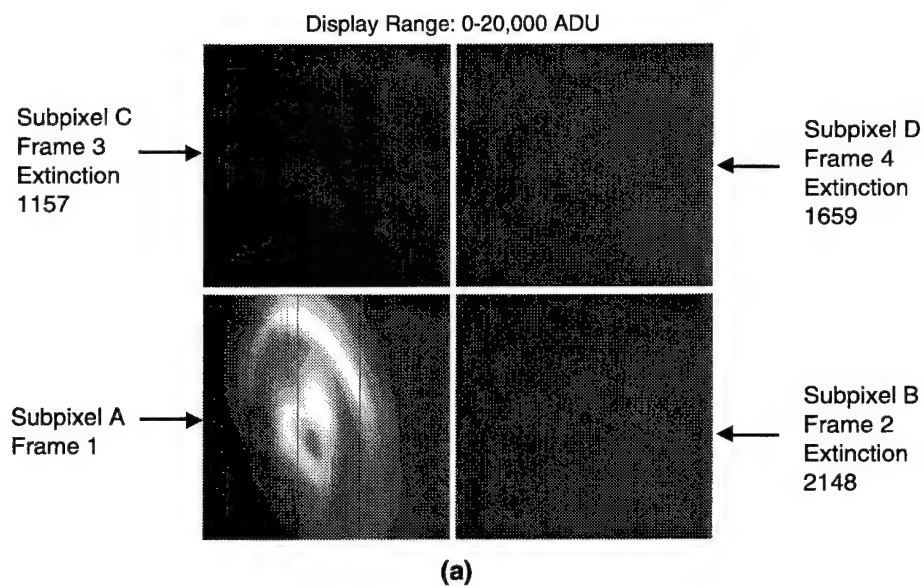
Figure 5-5. (a) Intensity images of four subpixels separated in post-processing. The LED flashed in frame 1. (b) Signal vs row position. Subpixel A (frame 1, high signal) repeats every fourth row.

29

6. ANALOG DEVICE TECHNOLOGY

6.1 EFFECT OF ANODIZATION ON SUPERCONDUCTIVE CIRCUITS

Superconductive electronics have long been a promising candidate for digital processing at clock speeds of 50–100 GHz. Until recently [1], their promise has had to remain just that—a promise—because of the absence of reliable fabrication technology. The most difficult demand to satisfy in the processing technology is the cross-chip device parameter variation: this requirement depends on the complexity of the circuit that is required. For petaflop computing applications, for example, the distribution of critical current values across a single chip must have a standard deviation of less than 1.5% in order for the bit-error rate to be acceptable [2]. Making development of such a processing technology even more difficult is the need to cool to 4.2 K for device testing, meaning that in-process device parameter shifts are difficult to identify.

In the course of post-process room-temperature testing [3], however, we identified a cross-wafer shift in critical current density J_c, shown in Figure 6-1, that was almost certainly due to an in-process shift. Because the trilayer deposition tool has a strong radial symmetry in the metal deposition and a highly uniform oxidation process, the observed nearly linear gradient in J_c could not be explained based on effects occurring during the barrier-oxide formation. When a short anodization step was included after the deposition of the junction counterelectrode, however, the linear gradient disappeared and was replaced by a large ellipsoidal distribution, askew relative to the wafer flat, with a much smaller range of J_c values and a highly uniform "sweet spot" near the wafer center. The full-range cross-wafer distribution of J_c was reduced from ±19% to ±12%. This general pattern was repeated several times across several different sets of wafers.

The fact that anodization leads to a drastic improvement in the J_c distribution invites the question: where did the processing shift originate? No unambiguous answer has presented itself, 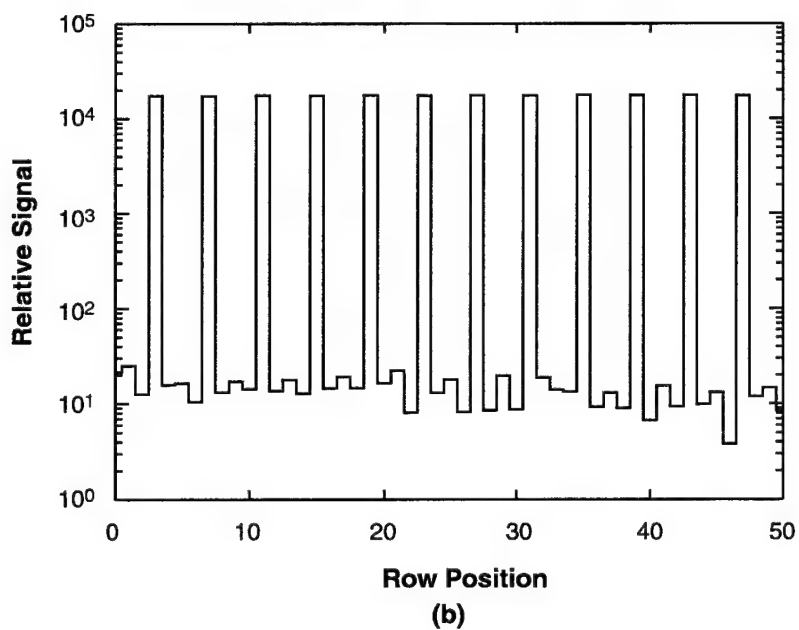but the fact that the problem was solved using anodization suggests that there is an attack of the junction that occurs from around its perimeter, where the anodic oxide would presumably retard chemical attack. To determine the source of the in-process shift in J_c values observed when no anodization step is included in the process, all the steps in which direct chemical attack of our barrier could occur are itemized in Table 6-1. The table lists processes occurring after the anodization step, but before the junction is sealed in by the oxide and in which the barrier is exposed to the environment. Because the observed shift has a linear gradient across the wafer, we can rule out all processes in which the symmetry is not linear or there is no reactive chemical used. The hexamethyldisilazane (HMDS) application process remains as a possible problem. We have found that exposure to HMDS decreases the sheet resistance of thin aluminum films. Further investigation of the mechanism of this attack is therefore warranted.
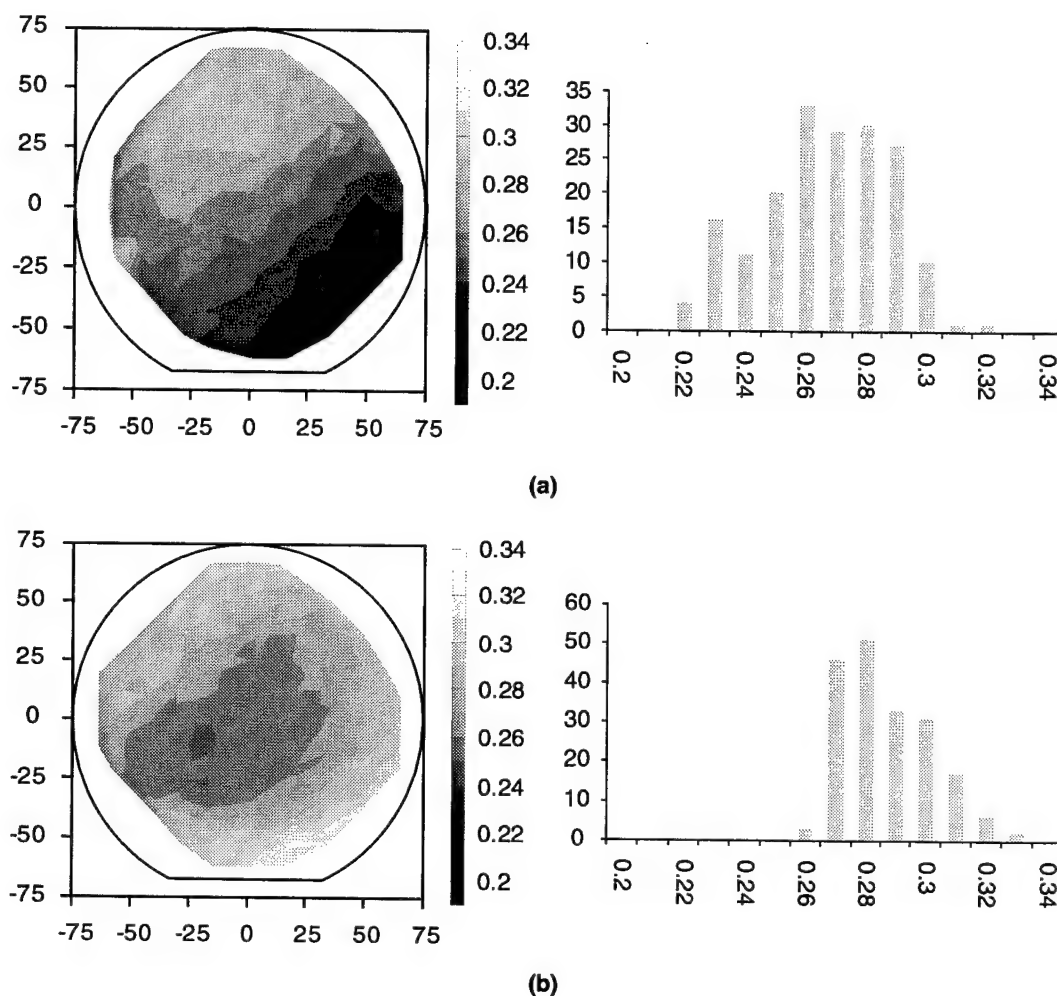
Figure 6-1. (a) Room-temperature tunneling resistance of distribution of 10 ×10-μm Josephson junctions across Nb/Al/AlO$_x$/Nb trilayer after processing, shown as both wafer map and histogram. This resistance is inversely proportional to the critical current density. (b) Same data collected from wafer processed in conjunction with the one in (a), but given a short anodization immediately after the definition of the junction counterelectrode. The cross-wafer standard deviation of critical current density dropped from 7.9% in the unanodized case to 5.4% in the anodized case. The cross-wafer critical current density range dropped from ±19% to ±12%.

TABLE 6-1

Steps in Which Direct Chemical Attack of Barrier Could Occur

Step	Symmetry	Chemical
Resist strip	Homogeneous	ACT 935
Dump rinse	Linear	DI H_2O
Spin-rinse-dry	Radial	DI H_2O
Base-electrode lithography		
Adhesion promotion	Linear	HMDS
Resist application	Radial	SPR-511A
Oxide deposition	None	SiH_4 and N_2O

As a direct consequence of the improved cross-wafer distribution, the cross-chip distribution of critical current density was also improved. In 100% of the chips tested with a critical current density of 10 kA/cm^2, the cross-chip critical current density varied by <1%. This level of cross-chip uniformity in critical current density is required for any process with which one hopes to generate highly integrated 100-GHz clock speed, Josephson junction based electronics.

K. K. Berggren   E. M. Macedo
D. Nakada   M. O'Hara

REFERENCES

1. K. K. Berggren, E. M. Macedo, D. A. Feld, and J. P. Sage, *IEEE Trans. Appl. Supercond.* **9**, 3271 (1999).

2. "Superconductor devices for ultrafast computing," in *Applications of Superconductivity*, H. Weinstock, ed. (Kluwer, Dordrecht, 2000), pp. 247-293.

3. M. J. O'Hara and K. K. Berggren, *IEEE Trans. Appl. Supercond.* **10**, 1669 (2000).

7. ADVANCED SILICON TECHNOLOGY

7.1 MONOLITHIC 3.3-V CCD/SOI-CMOS IMAGER TECHNOLOGY

Fully integrated image sensors, or "camera-on-a-chip" sensors, which monolithically combine image capture, support electronics, and analog-to-digital (A/D) conversion, have many systems applications where power, weight, and size are severely constrained. Though charge-coupled device (CCD) imagers have superior temporal read noise and spatial pattern noise, as well as higher optical fill factor compared to active-pixel sensors (APSs), high-performance CCDs have tended not to have high levels of support circuitry integrated on-chip.

In this report, we demonstrate a monolithic 3.3-V CCD/silicon-on-insulator–CMOS (SOI-CMOS) technology capable of delivering a "system on a chip" suitable for scientific or remote applications. The operating voltage was selected to allow both reasonable CCD well capacity and low CMOS power dissipation. As illustrated in Figure 7-1, the SOI starting material permits fabrication of bulk imaging devices (APSs or CCDs) in close proximity to, yet isolated from, fully depleted SOI (FDSOI) CMOS circuits. FDSOI CMOS characteristically achieves low-power operation because of its very thin depleted channel and reduced device parasitic capacitances [1]. The buried-oxide (BOX) isolation limits cross-talk between the bulk sensor and the CMOS circuitry, and also permits the bulk wafer resistivity to be tailored to the imaging requirements. The advantages of electrical isolation plus the greater radiation hardness of SOI compared to conventional CMOS were recognized several years ago in a feasibility study on the integration of SOI CMOS with PIN diodes in high-resistivity handle wafers for nuclear particle detectors [2].
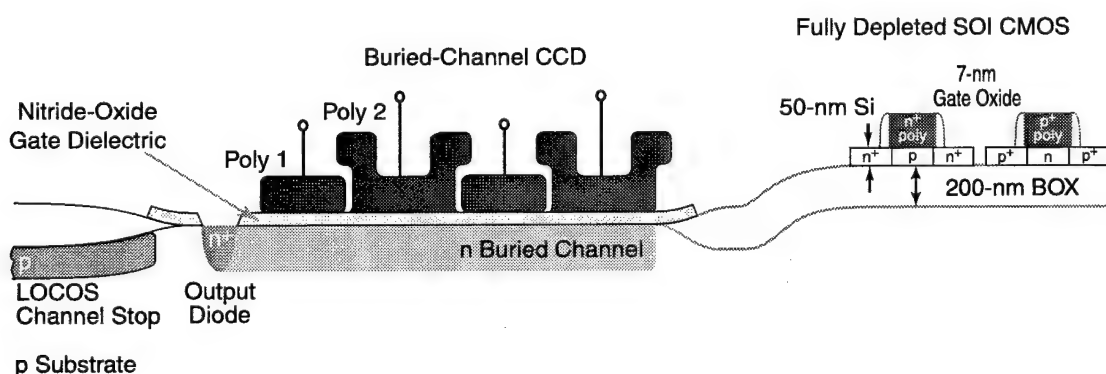
Figure 7-1. Schematic cross section illustrating merged CCD/SOI-CMOS technology. Imaging devices and FDSOI CMOS are fabricated in the same bonded SOI wafer. High-resistivity substrates are used for broad spectral response. The technology has been demonstrated by fabrication of a 128 × 128, 8 × 8-μm-pixel imager with on-chip 3.3-V clocking and A/D conversion.

35

TABLE 7-1
Process Parameters for CCD/SOI-CMOS Technology

Starting material	Unibond SOI
Bulk resistivity	300–5000 Ω cm
SOI CMOS L_{Gate}	0.35 μm
Minimum CCD pixel	$2 \times 2 \ \mu m^2$
CCD gate overlap	0.10–0.25 μm
CMOS gate oxide	7.2 nm
CCD gate dielectric	30/20/10 nm (oxide/nitride/oxide)
SOI thickness	50 nm at completion
BOX thickness	200 nm
SOI CMOS (source/drain/gate)	n^+ or p^+ doped $CoSi_2$
Bulk device isolation	LOCOS
SOI device isolation	Mesa
No. of metal layers	3

The SOI material for this process is Unibond™ wafers from SOITEC, made with high-resistivity epitaxial or bulk float-zone substrates to enable broad CCD spectral response. These bonded substrates were selected after a preliminary study of CCDs fabricated in several candidate SOI handle wafers [3]. Process parameters and integrated process flow are briefly summarized in Tables 7-1 and 7-2, respectively. All layers are defined with 248-nm KrF lithography and plasma-etch techniques to achieve 0.35-μm gate definition. The SOI and BOX are selectively removed from the wafer to permit CCD fabrication in the bulk handle wafer. For fully depleted CMOS operation, the SOI layer is reduced from 180 nm to its final 50-nm thickness by oxidation. Isolation for bulk devices is by local oxidation of silicon (LOCOS) and for SOI devices by mesa definition. The gate dielectric for the CCDs is a composite oxide/nitride stack and for CMOS is a 7.2-nm oxide.

The CCD is a two-poly, overlapping gate device with an n^- buried channel formed with either a phosphorus or arsenic implant. The SOI n-MOS channel is implanted with BF_2 and the SOI p-MOS channel with phosphorus. The first polysilicon layer (poly 1) is in-situ doped and is only defined in the bulk imaging regions. The second polysilicon layer (poly 2) is deposited undoped and is defined in both bulk and SOI regions; it is phosphorus-doped n^+ in the bulk region and complementarily doped (As or BF_2) in the SOI region. An all-dry poly-2 etch removes stringers resulting from CCD topography, while patterning 0.35-μm CMOS gates without breaking through the thin gate oxide. For the SOI CMOS we use a drain-extension doping designed to control the parasitic bipolar effect that otherwise would cause high off-state

TABLE 7-2
Process Flow for CCD/SOI-CMOS Technology

Bulk area definition, etch
Bulk sacrificial/SOI thinning oxidation
Bulk active area definition
Bulk device implants
Poly-1 definition and oxidation
SOI CMOS active area definition
SOI CMOS body doping
Poly-2 definition
Light/medium drain doping
Spacer formation
Source/drain/gate implant and rapid thermal anneal
Co-silicide formation
Dielectric deposition and chemical-mechanical planarization
Bulk contact hole etch
SOI contact hole etch
Damascene plug formation
Three-layer metallization
Passivation layer deposition, bonding pad openings
Sinter

current and an exponential increase in drain current at the higher drain voltages. Poly 2 is complementarily doped for CMOS devices and n^+ doped for bulk devices. To preserve submicron CMOS transistor behavior, rapid thermal annealing is used for dopant activation. Self-aligned 25-nm $CoSi_2$ (salicide) is formed on poly-2 and SOI source-drain regions. For the back-end processing we begin with a chemical-mechanical planarized, chemical-vapor deposited oxide followed by a three-layer-metal interconnect, with damascene vias and overglass. In addition to the integrated CCD sensor, we have also fabricated on the same wafer some exploratory APSs, which are described elsewhere [4].

Primary SOI device characteristics are presented in Table 7-3. The drain-induced barrier lowering observed with the n-MOS devices is a consequence of the SOI floating-body effect; this effect can be reduced with an H-gate or body-contacted structure. The device drive currents are a result of drain engineering to control the parasitic lateral bipolar transistor at the relatively high 3.3-V operating voltage.

37

TABLE 7-3
Fully Depleted SOI-CMOS Device Data

	n-MOS	p-MOS
L_g (μm)	0.35	0.35
V_{th} (V), V_{DS} = 50 mV	+0.46	−0.35
V_{th}^* (V), V_{DS} = 3.3 V	+0.26	−0.31
Subthreshold slope (mV/decade)	67	67
I_{Dsat}, $V_{DS} = V_{GS}$ = +3.3 V (μA/μm)	408	245
g_{msat} (mS/mm)	136	104
Junction capacitance (aF/μm^2)	186	186
*H-gate or body-tied configurations can be used to minimize the threshold shift created by the floating body.		

Figures 7-2(a) and 7-2(b) show typical SOI transistor subthreshold and output characteristics for devices with W/L = 8/0.35 μm. Note particularly that the *n*-MOS devices can withstand at least 4-V drain bias with no indication of punchthrough.

Figure 7-3 shows the stage delay for a typical 101 stage (fanout = 1) 0.35-μm gate length ring oscillator as a function of power supply voltage for the Lincoln Laboratory CCD/FDSOI-CMOS process (open circles) and for a commercial 0.35-μm gate length 3.3-V bulk CMOS process (open diamond). For digital 3.3-V operation, the CCD/SOI-CMOS technology demonstrates almost twice the speed of the bulk process (48 vs 93 ps/stage).

The use of precision 248-nm lithography enables much finer gate definition and level-level alignment than typical CCD processes. Figure 7-4 shows scanning electron micrograph cross sections of 5- and 2-μm pixel imagers with 0.25- and 0.10-μm nominal gate overlaps. The small overlaps minimize gate capacitance and thus drive power.

Figure 7-5 compares the dark current of a device from our standard bulk CCD process with that from one fabricated in the CCD/CMOS technology, using a SOI bonded epi substrate wafer. The results suggest that the bonding process needed to manufacture the SOI, as well as the CCD/CMOS fabrication, have not significantly degraded the substrate wafer quality.
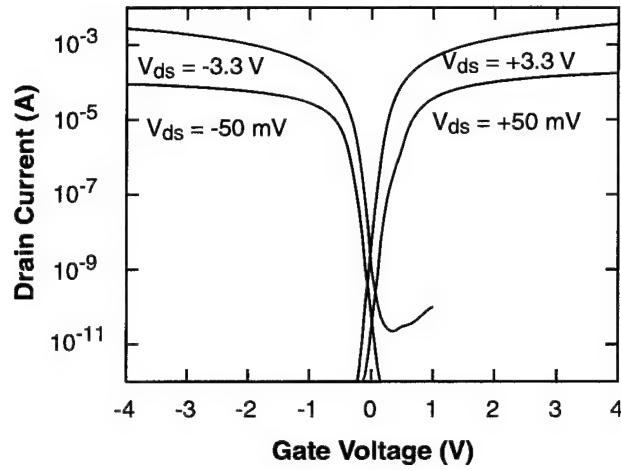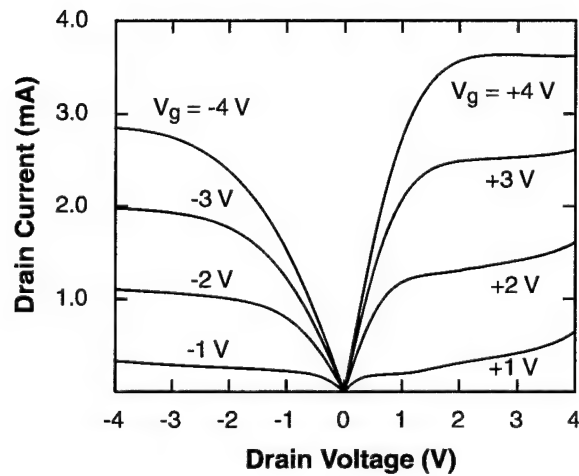
Figure 7-2. (a) Transfer characteristics for n-MOS and p-MOS devices. The use of complementarily doped poly 2 creates symmetric thresholds for n- and p-channel devices. W/L = 8/0.35 μm. (b) Output characteristics for n-MOS and p-MOS devices. Modifications in gate length and drain extension successfully forestall the parasitic bipolar effect that would create an exponential increase in drain current. W/L = 8/0.35 μm.
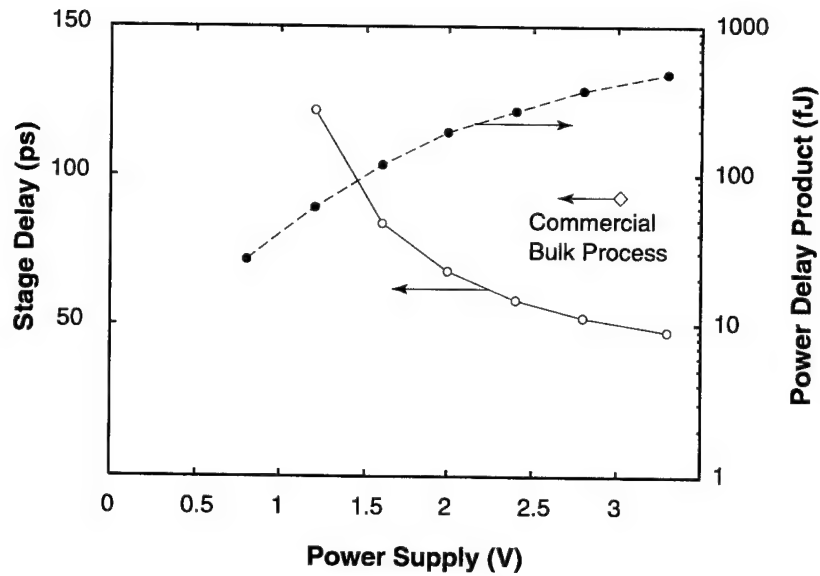
Figure 7-3. Stage delay (open circles) and power delay product (filled circles) per transition as functions of power supply voltage for a 101 stage ring oscillator (fanout = 1) fabricated in the CCD/SOI-CMOS process.

(a)

(b)
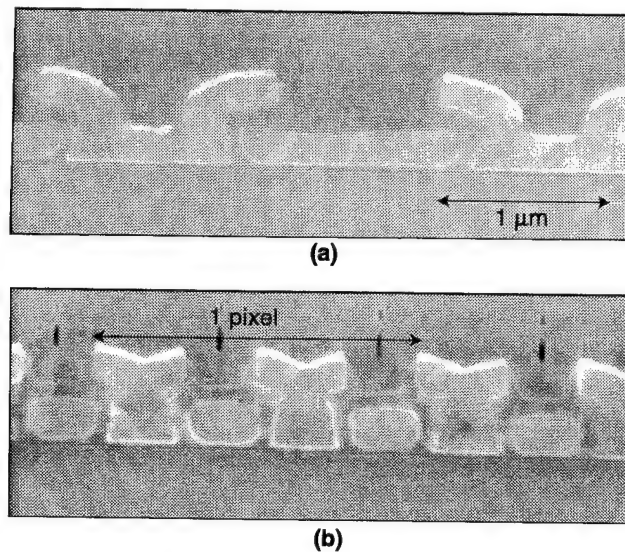
Figure 7-4. Scanning electron micrograph cross sections (HF-decorated) through four-phase (a) 5-µm-pixel and (b) 2-µm-pixel CCD imagers. Gate overlap on the 5-µm-pixel device shown is 0.25 µm and on the 2-µm-pixel device is 0.10 µm.

40
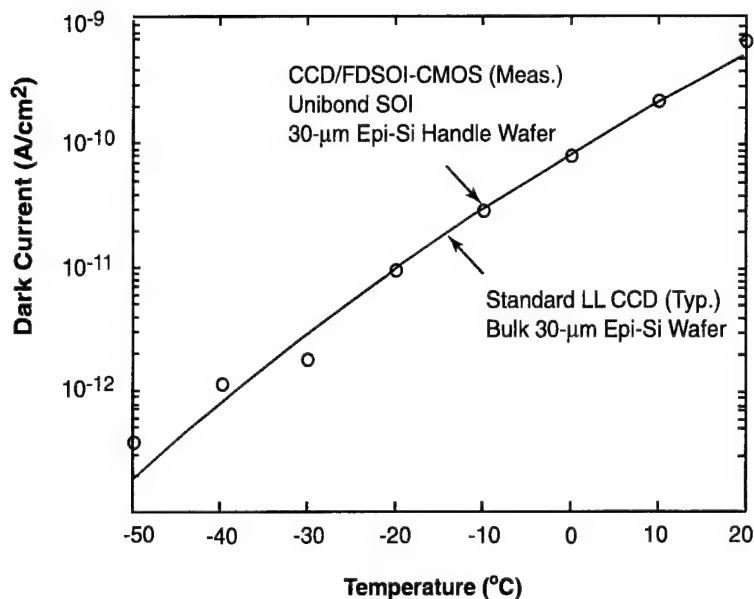
Figure 7-5. CCD dark current for imagers fabricated in a SOITEC/epi Si handle wafer (open circles) and for the standard Lincoln Laboratory bulk CCD process (solid line). Both substrates are 300-Ω cm, 30-μm epi silicon on Czochralski.

The charge-transfer inefficiency (CTI) generally remains low down to clock voltages below 2 V with no indication of spurious pockets or barriers in the channel potential beneath the gate junctures. The CTI at low signal levels was measured as a function of clock swing with a Fe[55] source (1620 e^-) on a three-phase, 15×15-μm pixel device, and the results are shown in Figure 7-6. The data here were taken at –50°C to ensure low background charge (<20 e^-/pixel/frame) during image integration and thus ensure a sensitive test for low concentration of traps. This device is of particular note because the handle wafer was 5000-Ω cm float-zone material. Such high purity is of interest for applications such as near-infrared imaging that require deep depletion. In addition we find that both the Unibond wafer preparation and our subsequent device processing do not induce significant numbers of slip dislocations. Float-zone silicon is prone to such defect formation during high-temperature processing.

Figure 7-7 shows the charge-handling capacity measured on 5×5-μm-pixel and 8×8-μm-pixel four-phase CCDs. The 8-μm-pixel device was driven with on-chip SOI-CMOS clocking; its well capacity at 3 V is in excess of 100,000 electrons—comparable to that of conventional CCD imagers at 10 V but with significant reduction in power consumption. Figure 7-8 shows an image obtained with this CCD operated with on-chip clocking.

41

We have fabricated for the first time an integrated image sensor consisting of a 128×128-pixel imager with 8×8-μm pixels, a charge-domain A/D converter [5], and all support circuitry. Since the design was not optimized for this process, the first pass results have 3–4 bits of resolution; a targeted 10–12-bit design is in progress. Figure 7-9 shows an image from this sensor operating at 3.3 V.

We have presented a technology capable of building a fully integrated low-power CCD sensor system. CCD charge-handling capability and charge transfer at 3 V are comparable to devices with much higher operating voltages, and FDSOI offers fast CMOS circuitry for digital and analog processing. A monolithic CCD/CMOS image sensor with on-chip A/D converter has been demonstrated.

V. Suntharalingam   B. Burke
M. Cooper   D. Yost
P. Gouker   M. Anthony
H. Whittington   J. Sage
J. Burns   S. Rabe
C. Chen   J. Knecht
S. Cann   P. Wyatt
C. Keast

REFERENCES

1. J.-P. Colinge, *Silicon-on-Insulator Technology: Materials to VLSI*, 2nd ed. (Kluwer Academic, Norwell, Mass., 1997), pp. 123-192.

2. B. Dierickx, D. Wouters, G. Willems, et al., *IEEE Trans. Nucl. Sci.* **40**, 753 (1993).

3. V. Suntharalingam, B. E. Burke, C. K. Chen, M. J. Cooper, and C. L. Keast, *Proceedings of the 2000 IEEE International SOI Conference* (IEEE, Piscataway, N.J., 2000), p. 136.

4. X. Zheng, C. Wrigley, G. Yang, and B. Pain, *Proceedings of the 2000 IEEE International SOI Conference* (IEEE, Piscataway, N.J., 2000), p. 138.

5. S. A. Paul and H-S. Lee, *Digest of Technical Papers: 1996 IEEE International Solid-State Circuits Conference* (IEEE, Piscataway, N.J., 1996), p. 188.
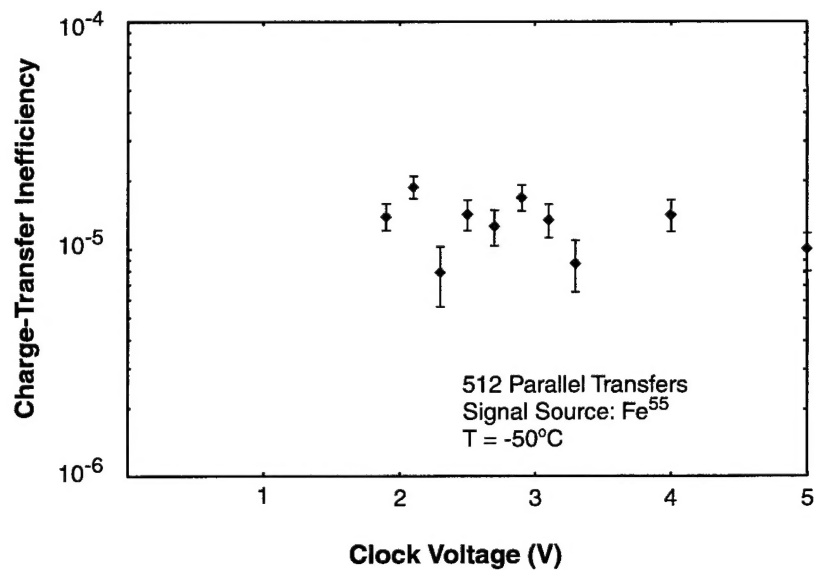
Figure 7-6. Charge-transfer inefficiency as a function of clocking voltage. Measurements were made on a 15-µm-pixel imager at –50°C.
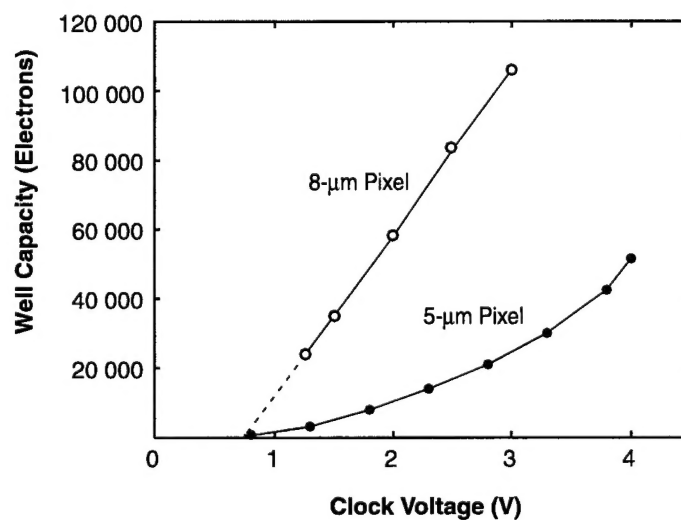
Figure 7-7. Charge-handling capacity of 8 × 8-µm-pixel and 5 × 5-µm-pixel four-phase imagers fabricated in the low-voltage CCD/SOI-CMOS process. The 8-µm pixel device was operated with on-chip clocking.

Figure 7-8. Sample image acquired by CCD/SOI-CMOS device with on-chip clocking and off-chip A/D conversion. CCD imager is a 128 ×128 array of 8 × 8-µm pixels which operates at 1.9–3.3 V.
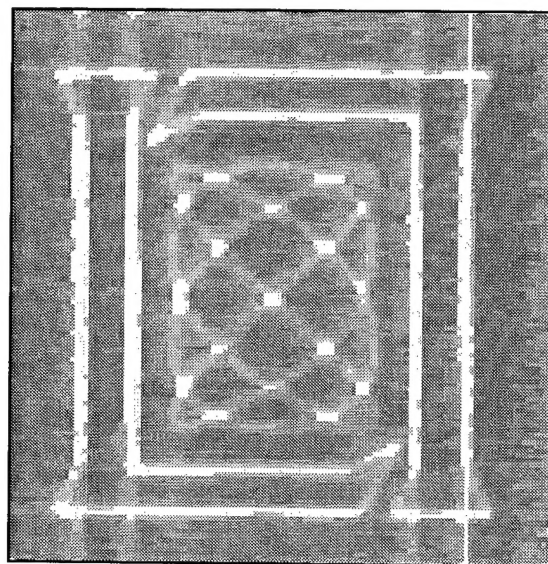
Figure 7-9. Sample image acquired by monolithic CCD/SOI-CMOS device with on-chip A/D conversion and clocking. CCD imager is a 128 × 128 array of 8 × 8-µm pixels operated at 3.3 V.

44

REPORT DOCUMENTATION PAGE

Form Approved
OMB No. 0704-0188

1. AGENCY USE ONLY (*Leave blank*)	2. REPORT DATE 15 February 2001	3. REPORT TYPE AND DATES COVERED Quarterly Technical Report, 1 November 2000–31 January 2001

4. TITLE AND SUBTITLE

Solid State Research

5. FUNDING NUMBERS

C — F19628-00-C-0002

6. AUTHOR(S)

David C. Shaver

7. PERFORMING ORGANIZATION NAME(S) AND ADDRESS(ES)

Lincoln Laboratory, MIT
244 Wood Street
Lexington, MA 02420-9108

8. PERFORMING ORGANIZATION REPORT NUMBER

2001:1

9. SPONSORING/MONITORING AGENCY NAME(S) AND ADDRESS(ES)

HQ Air Force Materiel Command
AFMC/STSC
Wright-Patterson AFB, OH 45433-5001

10. SPONSORING/MONITORING AGENCY REPORT NUMBER

ESC-TR-2000-074

11. SUPPLEMENTARY NOTES

None

12a. DISTRIBUTION/AVAILABILITY STATEMENT

Approved for public release; distribution is unlimited.

12b. DISTRIBUTION CODE

13. ABSTRACT (*Maximum 200 words*)

This report covers in detail the research work of the Solid State Division at Lincoln Laboratory for the period 1 November 2000–31 January 2001. The topics covered are Quantum Electronics, Electro-optical Materials and Devices, Submicrometer Technology, Biosensor and Molecular Technologies, Advanced Imaging Technology, Analog Device Technology, and Advanced Silicon Technology. Funding is provided by several DoD organizations—including the Air Force, Army, BMDO, DARPA, Navy, NSA, and OSD—and also by the DOE, NASA, and NIST.

14. SUBJECT TERMS

quantum electronics	biosensor technology	advanced silicon technology	CCD imager
electro-optical devices	molecular technology	lasers	superconductive circuits
materials research	advanced imaging technology	ion mobility spectrometer	CCD/SOI-CMOS technology
submicrometer technology	analog device technology	B-cell lines	

15. NUMBER OF PAGES
68

16. PRICE CODE

17. SECURITY CLASSIFICATION OF REPORT	18. SECURITY CLASSIFICATION OF THIS PAGE	19. SECURITY CLASSIFICATION OF ABSTRACT	20. LIMITATION OF ABSTRACT
Unclassified	Same as Report	Same as Report	Same as Report

NSN 7540-01-280-5500

Standard Form 298 (Rev. 2-89)
Prescribed by AMSI Std. 239-18
298-102